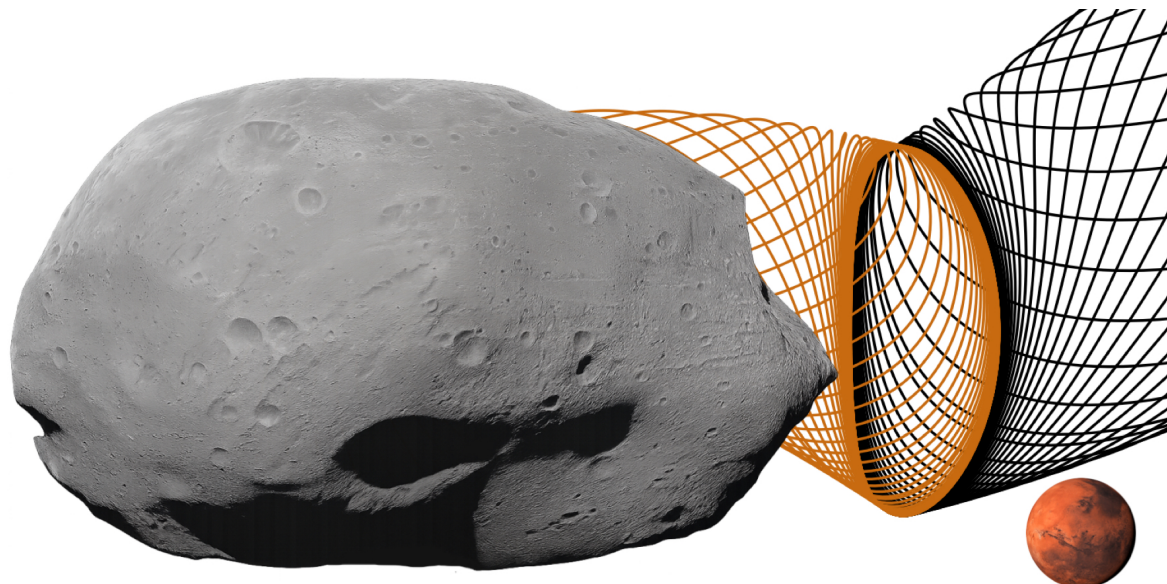

Bachelor's Thesis in Mathematics

Modeling impact dynamics of low-energy transit orbits on Phobos



Gunnar Montseny Gens

Academic supervisor: Dr. Josep J. Masdemont Soler

Administrative supervisor: Dr. Josep Maria Mondelo González

Submission: July 2025

Abstract

While the 9 km-wide Stickney crater on the Martian moon Phobos is widely believed to have formed from the impact of a celestial body, the exact details of its formation remain uncertain. This thesis investigates the potential role of sustained impacts from Martian ejecta in shaping the crater's current morphology. Specifically, the present study models the low-energy dynamics of dust particles in the Mars–Phobos system using the Circular Restricted Three-Body Problem (CR3BP). The phase space around the equilibrium point L_1 of the Mars–Phobos system is analyzed, as its associated invariant manifolds govern low-energy natural transport mechanisms between Mars and Phobos.

The parameterization method is employed to compute higher-order approximations of the invariant manifolds near L_1 . In addition, a Python code is developed to determine planar transit orbits for different energy levels. Numerical integration of these orbits suggests a plausible connection between their impacts on Phobos and the location of the Stickney crater. Future work should extend this analysis to include nonplanar transit orbits and implement energy-dependent dust particle density distributions.

Acknowledgements

I would like to express my deepest appreciation to Dr. Masdemont for his invaluable dedication and support throughout this project. His expertise and insightful feedback have been instrumental, and his mentorship has helped me grow both as a scientist and as a person. I am also sincerely grateful to Dr. Mondelo for his guidance and advice whenever I needed it. Special thanks go to Ruilong Li for providing the Python code implementing the parameterization method used in this thesis.

Lastly, I would like to acknowledge the unconditional support of my friends and family, especially my parents, sister, and partner. Their constant belief in me helped me stay motivated through the most challenging moments of this thesis.

Contents

1	Introduction	4
2	The Mars-Phobos system	5
3	Circular Restricted Three-Body Problem	6
3.1	Synodic reference frame	6
3.2	Equations of motion	6
3.2.1	Newtonian formulation	7
3.2.2	Hamiltonian formulation	8
3.3	Jacobi Constant	8
3.4	Energy-constrained dynamics	9
4	Phase space topology near L_1	12
4.1	Linearized phase space near L_1	12
4.2	Stability and invariant manifolds of L_1	13
4.3	Equilibrium region of L_1 and types of orbits	14
5	The parameterization method	22
5.1	The invariance equation and the cohomological equations	22
5.2	Solving the cohomological equations	23
5.3	Application of the parameterization method	24
6	Methodology	27
6.1	Computation of the parameterization of invariant manifolds	27
6.2	Numerical integration of trajectories	27
6.3	Determination of planar transit orbits	27
7	Results	29
7.1	Horizontal Lyapunov orbits and their stable manifolds	29
7.2	Impact simulations of planar transit orbits	30
7.2.1	Impact simulations at a fixed energy	30
7.2.2	Impact simulation at different energies	31
8	Conclusions	33
9	Appendices	34
9.1	Linearization of F and diagonalization of $DF(0)$	34
9.2	Second order approximation of F	36
9.3	Impact velocities	37

1 Introduction

Phobos, one of the two moons orbiting Mars, has an immense crater named Stickney. Although the most widely accepted theory in the scientific community attributes its formation to the impact of a celestial body (Morbidelli 2023), there is no conclusive evidence regarding the exact process by which it was created. This thesis explores whether sustained bombardment of dust particles generated by Martian ejecta could have contributed to the formation of the Stickney crater.

The Three-Body Problem (TBP) has been a central topic of interest for centuries in celestial mechanics. It involves predicting the motion of three celestial bodies in space as they mutually interact through gravity. Newton's Second Law leads to a system of differential equations which is what we commonly refer to as the TBP. While the Two-Body Problem is integrable, the general TBP is not. Poincaré (1887) proved that the TBP is non-integrable, making it impossible to express its general solutions in terms of elementary functions.

However, restricted versions of the problem are easier to work with. One of them is the Circular Restricted Three-Body Problem (CR3BP), where it is assumed that the mass of the third body is negligible when compared to the other two. Therefore, the third mass has a negligible gravitational effect on the other two, which are assumed to move in a circular orbit around their center of mass. Modeling the solutions of the differential equations of the CR3BP becomes increasingly more tractable than the original TBP.

A suitable case in which the CR3BP can be applied is the Mars–Phobos system, where Mars and Phobos serve as the two massive bodies, and a dust particle (originating from Martian surface ejecta) is the third body, with negligible mass. The CR3BP offers a useful approximation for modeling the dynamics of such particles. This is crucial for the present study, as it enables the analysis and simulation of dust particles impacting Phobos.

Within the framework of the CR3BP, the motion of the Martian dust particles can be further understood through the geometry and topology of a 6-dimensional phase space, particularly via structures known as invariant manifolds. These manifolds act as 'space highways' that guide particles through different regimes of motion depending on their energy and initial conditions. They can be visualized as higher-dimensional tubes that channel the motion of particles through phase space. Intuitively, they operate very similarly to ocean currents in Earth, which transport algae and organisms from ocean to ocean.

In space, the Interplanetary Transport Network (ITN) is the set of invariant manifolds connecting different planets in the Solar System. Although the ITN is normally used for calculating spacecraft trajectories between planets to minimize fuel, it can also be applied to better understand the low-energy dust dynamics in the Mars–Phobos system. If a dust particle is found inside the appropriate invariant manifold (making the dust particle follow a transit orbit), it could naturally transition from an orbit around Mars to an impact on Phobos without requiring additional energy. Therefore, understanding these invariant manifolds and the transit orbits inside of them give us valuable and necessary insight to model the impacts of these dust particles on Phobos.

The objectives of this thesis are:

1. Analyze the topology of the invariant manifolds near L_1 and its implications on the types of orbits.
2. Understand and apply the parameterization method, a semi-analytical technique to

parameterize invariant manifolds.

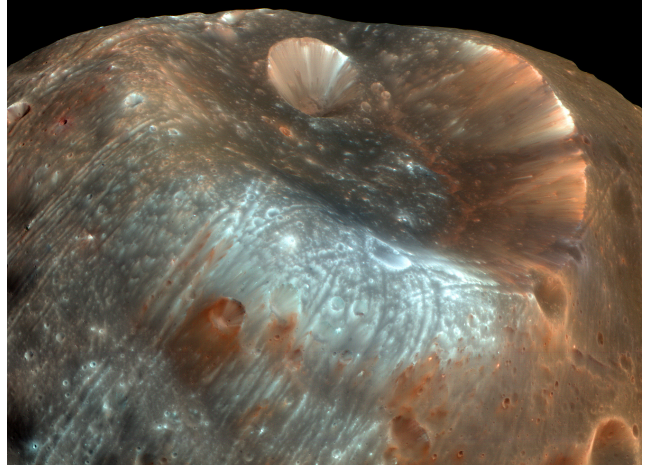
3. Numerically integrate and model planar transit orbits, and discuss impact dynamics on Phobos.

My primary contributions in this thesis are the numerical integration of low-energy trajectories in the planar CR3BP of the Mars-Phobos system, and the analysis of the phase space topology near Phobos. This involves identifying planar transit orbits that lead to collisions with Phobos, which requires a deep understanding of the structure of the invariant manifolds near Phobos. Although the Python code used to calculate higher-order approximations of these invariant manifolds was provided by my supervisor, I developed a clear intuition of the parameterization method to understand how local approximations are constructed and how they affect impact dynamics.

2 The Mars-Phobos system



(a) Phobos



(b) Stickney crater

Figure 1: Phobos and Stickney crater, pictures by the Mars Reconnaissance Orbiter. Image credit: (NASA/JPL/University of Arizona 2008).

Mars has two moons, one named Phobos and the other one named Deimos. Phobos has the approximate shape of a triaxial ellipsoid of size $27 \times 22 \times 18$ km, a density of 1.876 g/cm^3 and a low albedo of 0.07 (Ramsley et al. 2021). It has a semi-major axis of 9376 km around Mars and its orbital period is 7 h 39 minutes (NASA 2013). Its orbit is almost circular and planar, with a low eccentricity of $e = 0.0151$ and a low inclination of $i = 1.075^\circ$ (Ramsley et al. 2021).

The biggest crater on Phobos is Stickney crater, with a diameter of 9 km (Ramsley et al. 2021). Phobos is tidally locked in a synchronous rotation around Mars, meaning that the same side of Phobos is always facing Mars. It is precisely in this face that Stickney crater is found. Therefore, if there is Martian ejecta with enough energy to leave Mars' gravitational pull and hit Phobos, it probably hits Phobos in this side. Computing the invariant manifolds and transit orbits leading dust particles from orbiting Mars to impacting Phobos can tell us whether the observed location of the Stickney crater is influenced by natural low-energy transport mechanisms in the Mars-Phobos system.

3 Circular Restricted Three-Body Problem

This section presents the CR3BP, a simplification of the three-body problem where the third body is a particle that has a negligible mass compared to the mass of the other two bodies, otherwise known as the ***test particle***. The two main bodies will be called ***primaries***, and they are assumed to be rotating about their center of mass in a circular orbit. Due to the difference in mass, it is assumed the test particle will not exert any gravitational effect on the primaries.

Let M_1 and M_2 be the masses of primaries P_1 and P_2 such that $M_1 > M_2$, and let m_3 be the mass of the test particle. We assume that $m_3 \ll M_1, M_2$. Let a be the distance between the primaries' centers and T the orbital period of primaries P_1 and P_2 around their center of mass. In this thesis, the primaries are Mars (P_1) and Phobos (P_2), while the test particle is Martian ejecta in the form of a low-energy dust particle. For simplicity reasons, the units for mass, distance and time are normalized:

$$M_1 + M_2 \rightarrow 1, \quad a = 9376 \text{ km} \rightarrow 1, \quad T = 7 \text{ h } 39 \text{ min} \rightarrow 2\pi.$$

Note that the new nondimensional units can be converted back to SI units whenever necessary. These nondimensional units are essential to study the three-body system with just one parameter, called the **mass parameter** μ :

$$\mu \equiv \frac{M_2}{M_1 + M_2}. \tag{1}$$

In the Mars-Phobos system, $\mu = 1.66 \times 10^{-8}$.

3.1 Synodic reference frame

Let \mathfrak{R}_n be the rotating reference frame where the origin is set at the center of masses of the primaries and the x axis rotates counter-clockwise at rate $2\pi/T$ such that the primaries are always found on the x axis. Without loss of generality, let P_1 have a positive x coordinate and P_2 have a negative x coordinate. Since the center of mass is the origin, P_1 will be located at $(\mu, 0, 0)$ and P_2 will be located at $(\mu - 1, 0, 0)$. The z -axis is defined to be perpendicular to the orbital plane in which Mars and Phobos are found, and the y -axis is chosen so that the coordinate system of \mathfrak{R}_n is positively oriented. Figure 2 shows the (x, y) -space of \mathfrak{R}_n .

From now on, coordinates (x, y, z) describing the motion of the test particle will be with respect to \mathfrak{R}_n , unless otherwise specified. The next subsection presents the equations of motion of the CR3BP. Note that in \mathfrak{R}_n , also known as the ***synodic reference frame***, the equations of motion are autonomous. However, in a traditional inertial non-rotating frame, also known as the sidereal frame, the equations of motion are time-dependent.

3.2 Equations of motion

The equations of motion of the CR3BP can be derived and expressed in different mathematical formulations. Although they are equivalent, each of them offers specific advantages depending on the context. They are all used in different sections of this thesis for different purposes, which is why they are presented to the reader.

3.2.1 Newtonian formulation

After applying Newton's Second Law in \mathfrak{R}_n , the following differential equations describing the motion of the test particle (x, y, z, v_x, v_y, v_z) are found (see (Szebehely 1967) for full derivation):

$$\begin{aligned}\dot{x} &= v_x, & \dot{v}_x &= 2v_y + x - (1 - \mu)\frac{x - \mu}{r_1^3} - \mu\frac{x - (\mu - 1)}{r_2^3}, \\ \dot{y} &= v_y, & \dot{v}_y &= -2v_x + y - y\left(\frac{1 - \mu}{r_1^3} + \frac{\mu}{r_2^3}\right), \\ \dot{z} &= v_z, & \dot{v}_z &= -z\left(\frac{1 - \mu}{r_1^3} + \frac{\mu}{r_2^3}\right),\end{aligned}\tag{2}$$

where $v_x \equiv \dot{x}$, $v_y \equiv \dot{y}$, $v_z \equiv \dot{z}$, and r_1 and r_2 are the distances between the test particle and the primaries in \mathfrak{R}_n as shown in Figure 2. They can be calculated with:

$$r_1(x, y, z) = \sqrt{(x - \mu)^2 + y^2 + z^2}, \quad r_2(x, y, z) = \sqrt{(x - \mu + 1)^2 + y^2 + z^2}. \tag{3}$$

Since Eqs (2) are autonomous, an initial condition $(x^0, y^0, z^0, v_x^0, v_y^0, v_z^0)$ can be used to integrate the whole trajectory. Note that in this thesis, $(x, y, z, \dot{x}, \dot{y}, \dot{z})$ is the notation for the coordinates of the test particle in \mathfrak{R}_n .

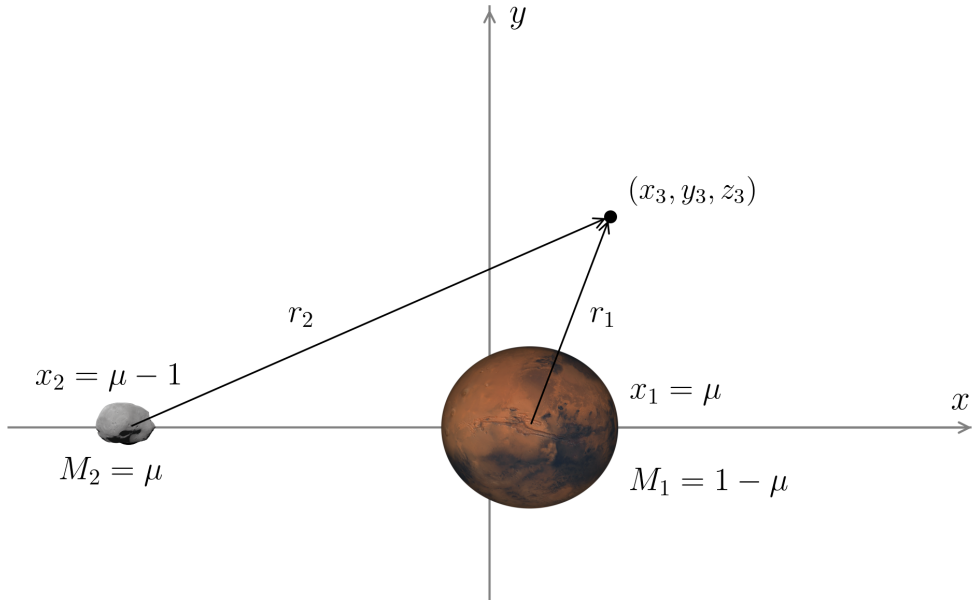


Figure 2: CR3BP's planar configuration in \mathfrak{R}_n with Mars as P_1 and Phobos as P_2 . The test particle has coordinates (x_3, y_3, z_3) in this plot, although (x, y, z) will be used moving forward for the test particles' coordinates. Distances and sizes not up to scale. Mars' image credit: NASA/JPL/Caltech/USGS, Phobos' image credit: ESA/DLR/FU Berlin (G. Neukum)

The equations of motion expressed in Eqs (2) can be equivalently written in a simpler form by introducing the effective potential, which takes into account the gravitational attraction of Mars and Phobos and the centrifugal effects of being in the rotating frame \mathfrak{R}_n .

Definition 3.1. Let x, y , and z be the position coordinates of a test particle in \Re_n . The **effective potential** Ω , evaluated at position (x, y, z) of the test particle, is defined as:

$$\Omega(x, y, z) = \frac{1}{2}(x^2 + y^2) + \frac{1-\mu}{r_1} + \frac{\mu}{r_2} + \frac{1}{2}\mu(1-\mu), \quad (4)$$

where r_1 and r_2 are defined in Eq (3).

The equations of motion can then be written as:

$$\ddot{x} - 2\dot{y} = \frac{\partial\Omega}{\partial x}, \quad \ddot{y} + 2\dot{x} = \frac{\partial\Omega}{\partial y}, \quad \ddot{z} = \frac{\partial\Omega}{\partial z}. \quad (5)$$

3.2.2 Hamiltonian formulation

The CR3BP admits a Hamiltonian formulation, which provides a different but equivalent way to express the equations of motion. The Hamiltonian describing the test particle in \Re_n is as follows (Gómez and Mondelo 2001):

$$H(x, y, z, p_x, p_y, p_z) = \frac{1}{2}((p_x + y)^2 + (p_y - x)^2 + p_z^2) - \Omega(x, y, z), \quad (6)$$

where p_x, p_y and p_z are the generalized momenta of the test particle. The Hamiltonian equations of the CR3BP that describe the motion of the test particle are (Koon et al. 2022):

$$\begin{aligned} \dot{x} &= \frac{\partial H}{\partial p_x} = p_x + y, & \dot{p}_x &= -\frac{\partial H}{\partial x} = p_y - \frac{1-\mu}{r_1^3}(x - \mu) - \frac{\mu}{r_2^3}(x - \mu + 1), \\ \dot{y} &= \frac{\partial H}{\partial p_y} = p_y - x, & \dot{p}_y &= -\frac{\partial H}{\partial y} = -p_x - \left(\frac{1-\mu}{r_1^3} + \frac{\mu}{r_2^3}\right)y, \\ \dot{z} &= \frac{\partial H}{\partial p_z} = p_z, & \dot{p}_z &= -\frac{\partial H}{\partial z} = -\left(\frac{1-\mu}{r_1^3} + \frac{\mu}{r_2^3}\right)z. \end{aligned} \quad (7)$$

Definition 3.2. A **first integral** of a system of differential equations is a function that remains constant along all solutions for as long as they exist. Such a function is also known as a constant of motion.

Remark 3.1. In \Re_n , the Hamiltonian H is a non-trivial C^1 first integral of the equations of motion of the CR3BP shown in Eq (7) (Szebehely 1967): H is a continuously differentiable function that remains constant along the trajectories of the CR3BP.

The equations of motion of the CR3BP have been expressed in different formulations but they all form an autonomous system in \Re_n . Note that the trajectory of the test particle can be described in a 6-dimensional phase space consisting of $(x, y, z, \dot{x}, \dot{y}, \dot{z})$ or (x, y, z, p_x, p_y, p_z) .

3.3 Jacobi Constant

The **Jacobi constant** or **Jacobi integral** is a first integral of the CR3BP. It is widely used in the astrodynamics community to quantify the energy associated with the test particle.

Definition 3.3. The Jacobi constant C_J is defined as:

$$C_J(x, y, z, \dot{x}, \dot{y}, \dot{z}) = 2\Omega(x, y, z) - (\dot{x}^2 + \dot{y}^2 + \dot{z}^2), \quad (8)$$

where $(x, y, z, \dot{x}, \dot{y}, \dot{z}) \in \Re_n$ are the coordinates of the test particle.

Proposition 3.1. C_J is a non-trivial C^1 first integral of the CR3BP.

Proof. Let us consider the Jacobi constant of a test particle with trajectory $(x(t), y(t), z(t), \dot{x}(t), \dot{y}(t), \dot{z}(t))$. We differentiate with respect to time:

$$\frac{d}{dt}C_J(x, y, z, \dot{x}, \dot{y}, \dot{z}) = 2\frac{d}{dt}\Omega(x, y, z) - 2\dot{x}\ddot{x} - 2\dot{y}\ddot{y} - 2\dot{z}\ddot{z}$$

Using Eq (5), we have:

$$\ddot{x} = 2\dot{y} + \frac{\partial\Omega}{\partial x}, \quad \ddot{y} = -2\dot{x} + \frac{\partial\Omega}{\partial y}, \quad \ddot{z} = \frac{\partial\Omega}{\partial z}.$$

Also, note that

$$\frac{d\Omega}{dt} = \dot{x}\frac{\partial\Omega}{\partial x} + \dot{y}\frac{\partial\Omega}{\partial y} + \dot{z}\frac{\partial\Omega}{\partial z}.$$

Combining the last two equations, we obtain $dC_J/dt = 0$. \square

Since C_J does not change during the trajectory of the test particle, it can be defined by the initial coordinates of the trajectory.

Remark 3.2. The Jacobi constant and the Hamiltonian are strongly related as $C_J = -2H$. Although the Hamiltonian H is not the traditional definition of energy (kinetic energy + potential energy), in this thesis H and C_J are referred to as the particle's energy. The quantities H and C_J can be used interchangeably, but note that when H increases, C_J decreases (and vice versa).

3.4 Energy-constrained dynamics

The motion of test particles takes place in a 6-dimensional phase space. However, if the value of C_J is fixed, then the trajectories are constrained to a 5-dimensional surface:

Definition 3.4. Given a fixed Jacobi constant $c_J \in \mathbb{R}$, its associated **energy surface** \mathcal{E} is defined as:

$$\mathcal{E}(c_J) = \{(x, y, z, \dot{x}, \dot{y}, \dot{z}) \in \mathfrak{R}_n \mid C_J(x, y, z, \dot{x}, \dot{y}, \dot{z}) = c_J\}. \quad (9)$$

Since C_J is a first integral, initial coordinates determine the energy of the trajectory, and the test particle always remains inside the same 5-dimensional energy surface. Fixing an energy also has restrictions on the 3-dimensional **configuration space** (space of all possible positions (x, y, z) of the system) of a particle's trajectory. Let us rearrange Eq (9):

$$\dot{x}^2 + \dot{y}^2 + \dot{z}^2 = 2\Omega(x, y, z) - C_J. \quad (10)$$

Since velocities represent physical quantities that must be real, the LHS of Eq (10) must be non-negative because it is a sum of real-valued squares. This imposes a constraint on the values the effective potential can have.

Definition 3.5. Consider a test particle with energy $c_J \in \mathbb{R}$. The **Hill's region** \mathcal{H} associated with c_J is a 3-dimensional surface defined as:

$$\mathcal{H}(c_J) = \{(x, y, z) \in \mathbb{R}^3 \mid 2\Omega(x, y, z) - c_J \geq 0\}. \quad (11)$$

The particle can only move freely within Hill's region, as it is energetically allowed to access this portion of the configuration space. The boundary of Hill's region is known as the ***Zero Velocity Surface*** (ZVS) in the CR3BP or ***Zero Velocity Curve*** (ZVC) in the planar CR3BP. Both correspond to the set of coordinates (x, y, z) for which $2\Omega(x, y, z) = c_J$. Thus, for $C_J = c_J$, the ZVC (or ZVS) separates Hill's region from the forbidden region of motion. Note that the complement of Hill's region in configuration space is referred to as the ***energetically forbidden region***.

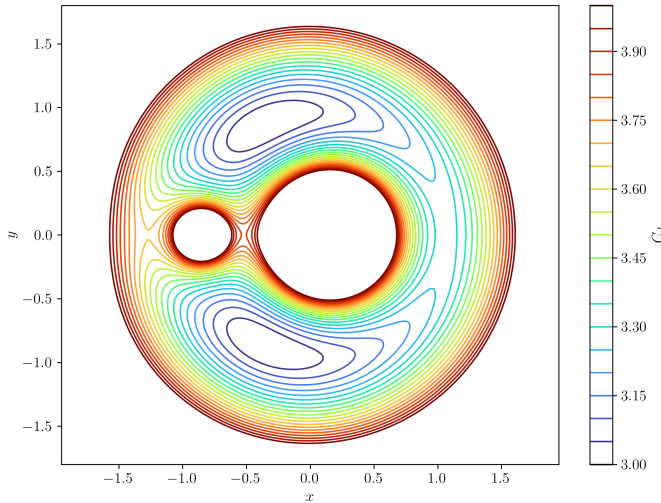


Figure 3: ZVC for different energy levels. $\mu = 0.15$ is used to better display the structure the ZVC. Primary 1 would be on the right white circular area and Primary 2 would be on the left white circular area.

Figure 3 shows the different ZVCs for different energies. As the Jacobi constant c_J increases, its corresponding $\mathcal{H}(c_J)$ is reduced. This is consistent with the fact that a higher Jacobi constant implies a lower particle energy. If the test particle has less energy, its energetically forbidden region is bigger, as it is harder for the particle to escape from the gravitational effect of the primaries.

A representation for the different energetically forbidden regions near Phobos is displayed in Figure 4. The higher the Jacobi constant, the larger its corresponding energetically forbidden region is. The idea is that the ZVCs act as a 'bottleneck' for low-energy test particles. A lower c_J implies a bigger bottleneck and an easier path for test particles to go from Mars to Phobos. Here, Mars' region refers to the space surrounding Mars bounded by the ZVC, and Phobos' region is defined analogously. Note that for $C_J = 3.0000281$, Phobos' region is no longer accessible from Mars' region, making impacts on Stickney impossible with this energy. For $C_J > 3.0000281$, low-energy dust particles orbiting Mars are energetically trapped in Mars' region and will never be able to transit to Phobos' region.

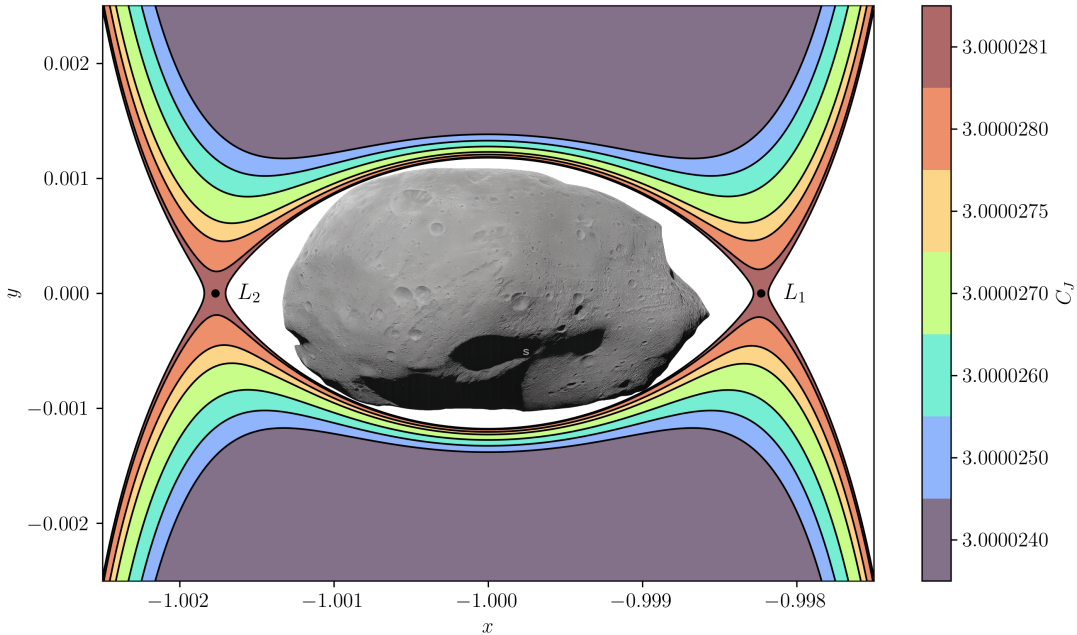


Figure 4: Shows the different energetically forbidden regions for 7 different energies in the Mars-Phobos system. Phobos is shown and Mars would be to the right of Phobos. Stickney crater is significantly visible on the top right of Phobos. The black lines represent the ZVCs for each energy. Note that the energetically forbidden regions of lower C_J s are displayed on top of the higher C_J energetically forbidden regions. Note that $x_{L_1} \approx -0.99823$. The image of Phobos was taken by the Mars Express HRSC, and image credit is for ESA/DLR/FU Berlin (G. Neukum).

In addition, Figure 4 shows a black dot located between Mars' region and Phobos' region, labeled L_1 and with energy $C_J(L_1) = 3.0000281$. This is one of the five equilibrium points of the CR3BP, also known as libration or Lagrange points. For completeness, the general definition of equilibrium points is given below:

Definition 3.6 (Equilibrium/fixed points). Let $\dot{x} = f(x)$ be an autonomous system of differential equations with $x \in \mathbb{R}^n$. Let $x_0 \in \mathbb{R}^n$. Then x_0 is an **equilibrium/fixed point** of $\dot{x} = f(x)$ if $f(x_0) = 0$.

There are five different Lagrange points, three of them in the x axis of \mathfrak{R}_n . These three are referred to as the collinear Lagrange points. As discussed in this section and shown in Figure 4, the ZVC create a bottleneck around L_1 , constraining the motion of particles between Mars' region and Phobos' region. The only way for a low-energy particle to go from Mars to Phobos is through this bottleneck.

This thesis focuses on the invariant manifolds associated with L_1 , which is located between Phobos and Mars. These invariant manifolds, which will be mathematically defined and analyzed in depth in Section 4, reveal that the dynamics around L_1 admit different types of trajectories. As a result, they control the natural transport of dust particles¹ orbiting around Mars that are able to cross the bottleneck and reach Phobos.

¹Martian ejecta

4 Phase space topology near L_1

Section 4.1 introduces the linearized phase space dynamics near L_1 , Section 4.2 introduces the invariant manifolds associated with L_1 , and Section 4.3 describes the types of orbits near L_1 . Since the linearized dynamics provide a first-order approximation of the nonlinear dynamics of the CR3BP around L_1 , they are topologically equivalent to the nonlinear dynamics only within a limited neighborhood of L_1 . This limited neighborhood is referred to as ***equilibrium region*** \mathcal{R}_1 , whose concept will be used throughout Section 4.1 and Section 4.2, and formally defined in Section 4.3.

4.1 Linearized phase space near L_1

Remark 4.1. Let $\dot{x} = f(x)$ be an autonomous nonlinear system of differential equation with $x \in \mathbb{R}^n$. Let $x_0 \in \mathbb{R}^n$ be an equilibrium point of $\dot{x} = f(x)$. Then the Jacobian matrix of $f(x)$ at x_0 , $A = Df(x_0) \in \mathbb{R}^{n \times n}$, provides the linearized system of $\dot{x} = f(x)$:

$$\begin{pmatrix} \dot{x}_1 \\ \dot{x}_2 \\ \vdots \\ \dot{x}_n \end{pmatrix} = \dot{x} = Ax = \begin{pmatrix} \frac{\partial f_1}{\partial x_1} & \frac{\partial f_1}{\partial x_2} & \cdots & \frac{\partial f_1}{\partial x_n} \\ \frac{\partial f_2}{\partial x_1} & \frac{\partial f_2}{\partial x_2} & \cdots & \frac{\partial f_2}{\partial x_n} \\ \vdots & \vdots & \ddots & \vdots \\ \frac{\partial f_n}{\partial x_1} & \frac{\partial f_n}{\partial x_2} & \cdots & \frac{\partial f_n}{\partial x_n} \end{pmatrix} \begin{pmatrix} x_1 \\ x_2 \\ \vdots \\ x_n \end{pmatrix}$$

To simplify the linearization of the equations of motion of the CR3BP, the origin of \mathfrak{R}_n is shifted to L_1 , and the coordinates are expressed as $X = (x, p_x, y, p_y, z, p_z) \in \mathfrak{R}_n$. The nonlinear terms of Eq (5) can be expanded into a power series around the equilibrium point L_1 (see Appendix 9.1). The equations of motion of the CR3BP can then be rewritten as an autonomous nonlinear system of differential equations such that $\dot{X} = F(X)$, where F is the vector field of the equations of motion of the CR3BP expanded around L_1 . In addition, Appendix 9.1 details how to obtain F , the Jacobian matrix of F at $X = 0$, denoted by $A = DF(0)$, and the eigenvalues and eigenvectors of A .

The six eigenvalues of A are given in the following set:

$$\Lambda_A = \{\lambda_0, -\lambda_0, w_h i, -w_h i, w_v i, -w_v i\},$$

where $\lambda_0, w_h, w_v \in \mathbb{R}^+$. Their corresponding eigenvectors, in the same order, are:

$$E_A = \{(v_{\lambda_0}, 0, 0), (v_{-\lambda_0}, 0, 0), (v_{w_h i}, 0, 0), (v_{-w_h i}, 0, 0), (0, 0, 0, 0, 1, 0), (0, 0, 0, 0, 0, 1)\},$$

where $v_{\lambda_0}, v_{-\lambda_0}, v_{w_h i}, v_{-w_h i} \in \mathbb{R}^4$ are calculated in Appendix 9.1.

Notation 4.1. From this point forward, the eigenvector of A associated with eigenvalue λ of A is denoted by u_λ .

4.2 Stability and invariant manifolds of L_1

The first step is to define the invariant manifolds associated with L_1 and prove their existence. These two tasks can be achieved by applying Theorem 4.1 to $\dot{X} = F(X)$. Before introducing Theorem 4.1, the concept of invariance must be defined:

Definition 4.1 (Invariant set for f , adaptation of Definition 1.39 in (Chicone 2006)). Let $\dot{x} = f(x)$ be an autonomous system of differential equations with $x \in \mathbb{R}^n$ and let $\phi_t(x_0)$ be a solution to $\dot{x} = f(x)$ such that $\phi_0(x_0) = x_0$. Let $S \subseteq \mathbb{R}^n$ be a set. Then S is an **invariant set for f** if for every $x_0 \in S$, solution $\phi_t(x_0) \in S$ for all values of t such that $\phi_t(x_0)$ exists.

Theorem 4.1 (Center Manifold Theorem, adaptation of Theorem 3.2.1 in (Guckenheimer et al. 1983)). *Let $\dot{x} = f(x)$ be a nonlinear autonomous system of differential equations with $x \in \mathbb{R}^n$ such that $f(0) = 0$. Let $A = Df(0) \in \mathbb{R}^{n \times n}$ be the Jacobian matrix, making $\dot{x} = Ax$ the new linearized system. Suppose eigenvalues of A can be divided into three subsets Λ_s , Λ_c and Λ_u such that:*

$$\begin{aligned}\Lambda_s &= \{\lambda \in \mathbb{C} \mid \det(A - \lambda I_n) = 0, \operatorname{Re} \lambda < 0\}, \\ \Lambda_u &= \{\lambda \in \mathbb{C} \mid \det(A - \lambda I_n) = 0, \operatorname{Re} \lambda > 0\}, \\ \Lambda_c &= \{\lambda \in \mathbb{C} \mid \det(A - \lambda I_n) = 0, \operatorname{Re} \lambda = 0\}.\end{aligned}$$

Let E^s , E^u and E^c be the eigenspaces of Λ_s , Λ_u and Λ_c respectively. Then:

1. There exists a manifold \mathcal{W}^s tangent to E^s at 0, called the **invariant stable manifold**.
2. There exists a manifold \mathcal{W}^u tangent to E^u at 0, called the **invariant unstable manifold**.
3. There exists a manifold \mathcal{W}^c tangent to E^c at 0, called the **invariant center manifold**.
4. Manifolds \mathcal{W}^s , \mathcal{W}^u and \mathcal{W}^c are invariant for f .

(Find proof in (Guckenheimer et al. 1983))

Theorem 4.1 is directly applied to the L_1 equilibrium point in the CR3BP, where $f = F$. In this case, $\Lambda_s = \{-\lambda_0\}$, $\Lambda_u = \{\lambda_0\}$ and $\Lambda_c = \{\pm w_h i, \pm w_v i\}$. The respective eigenspaces in our case are $E^s = \{u_{-\lambda_0}\}$, $E^u = \{u_{\lambda_0}\}$ and $E^c = \{u_{w_h i}, u_{-w_h i}, u_{w_v i}, u_{-w_v i}\}$. This application provides a natural definition for the invariant manifolds associated with L_1 .

Remark 4.2. Let $X_0 \in \mathcal{R}_1 \subset \mathbb{R}^6$. Let $\Phi_t(X_0)$ be a solution to $\dot{X} = F(X)$ with initial condition $\Phi_0(X_0) = X_0$.

- If $X_0 \in \mathcal{W}^s$, then it lies on the **local invariant stable manifold** tangent to $u_{-\lambda_0}$ at L_1 . Consequently, $\lim_{t \rightarrow \infty} \Phi_t(X_0) = 0$.
- If $X_0 \in \mathcal{W}^u$, then it lies on the **local invariant unstable manifold** tangent to u_{λ_0} at L_1 . Consequently, $\lim_{t \rightarrow -\infty} \Phi_t(X_0) = 0$.
- If $X_0 \in \mathcal{W}^c$, then it lies on the **local invariant center manifold** tangent to $\{u_{w_h i}, u_{-w_h i}, u_{w_v i}, u_{-w_v i}\}$ at L_1 . Consequently, $0 < |\Phi_t(X_0)| < \infty$ for all t such that $\Phi_t(X_0)$ exists.

Intuitively, the stable manifold is formed by all the trajectories that converge to the origin as $t \rightarrow \infty$, the unstable manifold consists of all the trajectories that converge to the origin as $t \rightarrow -\infty$, and the center manifold is formed by all the trajectories that are bounded and always stay close to the origin, but never converge to it either.

4.3 Equilibrium region of L_1 and types of orbits

This subsection formally defines the equilibrium region \mathcal{R}_1 , explores the topology of the linearized phase space of \mathcal{R}_1 , and discusses different types of motion that arise from it. Drawing on the conceptual foundations presented in (Gómez, Koon, et al. 2004) and (Koon et al. 2022), a problem-specific approach to the planar Mars-Phobos CR3BP is developed and adapted to the framework of this thesis to support the analysis presented in the Results section (Section 7).

Instead of using reference frame \mathfrak{R}_n , a new reference frame \mathfrak{R}_l is considered, with E_A as its eigenbasis and L_1 as its origin. The corresponding coordinates in \mathfrak{R}_l are denoted by s_i , for $i \in \{1, \dots, 6\}$. The equations of motion in \mathfrak{R}_l are:

$$\begin{aligned}\dot{s}_1 &= \omega_h s_2, & \dot{s}_2 &= -\omega_h s_1, \\ \dot{s}_3 &= \omega_v s_4, & \dot{s}_4 &= -\omega_v s_3, \\ \dot{s}_5 &= \lambda_0 s_5, & \dot{s}_6 &= -\lambda_0 s_6,\end{aligned}\tag{12}$$

where Eq (12) have been extracted from (Gómez, Koon, et al. 2004). The first four equations correspond to the 4-dimensional center manifold, while the bottom two represent a saddle (stable and unstable manifolds). The center manifold has a 2-dimensional planar projection and a 2-dimensional vertical projection, and they are independent from each other. Therefore, L_1 has the stability of what is commonly known as **center** \times **center** \times **saddle**.

According to Eq (12), s_1, s_2 parameterize the planar center manifold, s_3, s_4 the vertical center manifold, s_5 the unstable manifold, and s_6 the stable manifold. These coordinates allow the Hamiltonian H to be expanded as a power series around L_1 in \mathfrak{R}_l . Since L_1 is an equilibrium point, the linear term is zero, and the second-order approximation $H_{\leq 2}$ can be expressed as:

$$H_{\leq 2}(s_1, \dots, s_6) = H_0 + H_2(s_1, \dots, s_6) = -\frac{1}{2}C_J(L_1) + H_2(s_1, \dots, s_6),\tag{13}$$

where H_0 is the constant term and H_2 is the second-order term. The explicit expression of H_2 is derived in (Jorba et al. 1999), and is given by:

$$H_2(s_1, \dots, s_6) = \frac{w_h}{2}(s_1^2 + s_2^2) + \frac{w_v}{2}(s_3^2 + s_4^2) + \lambda_0 s_5 s_6.\tag{14}$$

Definition 4.2. Let $c_J \in \mathbb{R}$ be fixed. The **equilibrium region** \mathcal{R}_1 associated with c_J is defined as the neighborhood around L_1 such that:

$$\mathcal{R}_1(c_J) = \{(s_1, s_2, s_3, s_4, s_5, s_6) \in \mathfrak{R}_l \mid H_2(s_1, \dots, s_6) = \delta(c_J), |s_5 - s_6| \leq K_{c_J}\},\tag{15}$$

where $\delta(c_J) = \frac{1}{2}(C_J(L_1) - c_J)$, and $K_{c_J} > 0$ is chosen so that the linearized dynamics of $\mathcal{R}_1(c_J)$ are still topologically equivalent to the nonlinear dynamics of the CR3BP near L_1 . The precise determination of K_{c_J} , which varies with energy, is not addressed in this thesis.

The first condition in Eq (15) fixes the energy of the system, so it reduces the 6-dimensional phase space to a 5-dimensional energy surface $\mathcal{E}(c_J)$. The second condition limits the equilibrium region \mathcal{R}_1 in the (s_5, s_6) -space. To characterize the topology of \mathcal{R}_1 , the following definition is needed:

Definition 4.3 (n -sphere). An n -sphere with radius R and center coordinates c_1, \dots, c_{n+1} is defined as:

$$S^n(R) = \{(x_1, \dots, x_{n+1}) \in \mathbb{R}^{n+1} \mid \sum_{i=1}^{n+1} (x_i - c_i)^2 = R^2\}. \quad (16)$$

Proposition 4.1. Let $c_J \in \mathbb{R}$ be fixed. Then $\mathcal{R}_1(c_J)$ is homeomorphic to $S_{c_J}^4 \times I_{c_J}$ where $I_{c_J} \subset \mathbb{R}$ is an interval, and $S_{c_J}^4$ is a 4-sphere.

Proof. The first condition of Eq 15 can be rewritten as:

$$\frac{w_h}{2}(s_1^2 + s_2^2) + \frac{w_v}{2}(s_3^2 + s_4^2) + \frac{\lambda_0}{4}(s_5 + s_6)^2 = \delta(c_J) + \frac{\lambda_0}{4}(s_5 - s_6)^2. \quad (17)$$

Note that by definition, $s_5 - s_6 = k \in [-K_{c_J}, K_{c_J}] = I_{c_J}$. Let us define a function:

$$\begin{aligned} \phi : \mathcal{R}_1(c_J) &\longrightarrow S_{c_J}^4 \times I_{c_J} \\ (s_1, s_2, s_3, s_4, s_5, s_6) &\longmapsto \left(s_1\sqrt{w_h/2}, s_2\sqrt{w_h/2}, s_3\sqrt{w_v/2}, s_4\sqrt{w_v/2}, s_5\sqrt{\lambda_0}, k \right) \end{aligned}$$

The corresponding $S_{c_J}^4$ sphere has a radius of $R(c_J) = \sqrt{\delta(c_J) + \lambda_0 k^2/4}$ with center coordinates $(0, 0, 0, 0, \frac{k}{2}\sqrt{\lambda_0})$. By construction, ϕ is bijective and continuous, and its inverse can be found by reversing the multiplications into divisions, yielding a continuous bijective inverse. Therefore, ϕ is a homeomorphism. \square

Corollary 4.1. If $z, \dot{z} = 0$ or $s_3, s_4 = 0$ (planar CR3BP), then $\mathcal{R}_1 \cong S^2 \times I$.

Notation 4.2. Let $c_J \in \mathbb{R}$ be fixed. Let $J = \{i_1, \dots, i_p\} \subset \{1, \dots, 6\}$, with $p \leq 6$. Then $\pi_{c_J}^{i_1, \dots, i_p}$ is the projection of $\mathcal{R}_1(c_J)$ onto $\{(s_1, \dots, s_6) \in \mathfrak{R}_l \mid s_j = 0, j \notin J\}$.

The best way to understand the 6-dimensional phase space $\mathcal{R}_1(c_J)$ around L_1 is to do three projections of it, one describing the saddle projection $\pi_{c_J}^{5,6}$, another describing the planar center projection $\pi_{c_J}^{1,2}$, and another describing the vertical center projection $\pi_{c_J}^{3,4}$, as seen in Figure 5. Before diving into a thorough investigation of the topology of \mathcal{R}_1 , the following proposition is needed:

Proposition 4.2. $s_5 s_6$ ($s_5, s_6 \neq 0$), $s_1^2 + s_2^2$ and $s_3^2 + s_4^2$ are first integrals of Eq (12).

Proof. We use Eq (12) for all three derivations:

$$\begin{aligned} \frac{d}{dt}(s_5 s_6) &= \dot{s}_5 s_6 + s_5 \dot{s}_6 = \lambda_0 s_5 s_6 - \lambda_0 s_5 s_6 = 0. \\ \frac{d}{dt}(s_1^2 + s_2^2) &= 2s_1 \dot{s}_1 + 2s_2 \dot{s}_2 = 2w_h s_1 s_2 - 2w_h s_1 s_2 = 0. \\ \frac{d}{dt}(s_3^2 + s_4^2) &= 2s_3 \dot{s}_3 + 2s_4 \dot{s}_4 = 2w_v s_3 s_4 - 2w_v s_3 s_4 = 0. \end{aligned}$$

\square

Now, let us fix $C_J = c_J \in \mathbb{R}$, and understand the three projections of $\mathcal{R}_1(c_J)$ step by step:

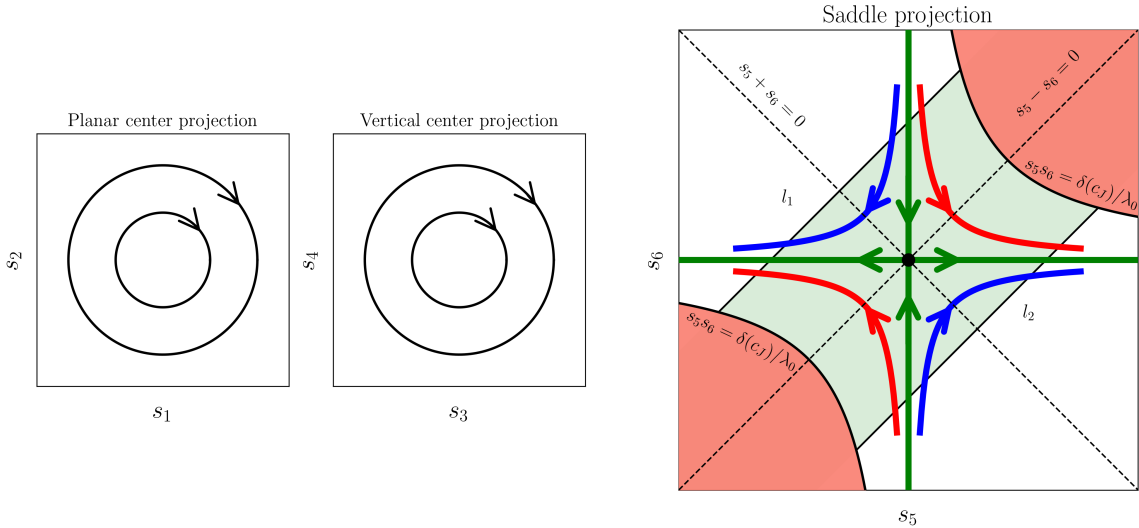


Figure 5: Stability of L_1 : center \times center \times saddle. It shows $\pi_{c_J}^{1,2}$ on the left, then $\pi_{c_J}^{3,4}$ in the middle and then $\pi_{c_J}^{5,6}$ on the right. The green arrows represent the asymptotic orbits \mathcal{A} , the black dot at the center represents the bounded orbits \mathcal{B} , the red arrows represent the transit orbits \mathcal{T} and the blue arrows represent the non-transit \mathcal{N} . The left of l_1 is Mars' region, while the right of l_2 is Phobos' region. The red area is the energetically-forbidden region, while the green area represents the projection of $\mathcal{R}_1(c_J)$ onto the (s_5, s_6) -space. Figure inspired by Figure 4 in (Gómez, Koon, et al. 2004).

- (i) For each point in the (s_5, s_6) -space, there is a corresponding 3-sphere in $\pi_{c_J}^{1,2,3,4}$. As c_J is fixed and s_5, s_6 are chosen too, the 3-sphere for coordinates (s_5, s_6) is given by:

$$S_{c_J}^3(s_5, s_6) = \{(s_1, s_2, s_3, s_4) \in \pi_{c_J}^{1,2,3,4} \mid \frac{w_h}{2}(s_1^2 + s_2^2) + \frac{w_v}{2}(s_3^2 + s_4^2) = \delta(c_J) - \lambda_0 s_5 s_6\}. \quad (18)$$

In the planar case with $s_3, s_4 = 0$, each point in the (s_5, s_6) -space corresponds to a 1-sphere in the projection of $\mathcal{R}_1(c_J)$ onto the (s_1, s_2) -space. It is defined as:

$$S_{c_J}^1(s_5, s_6) = \{(s_1, s_2) \in \pi_{c_J}^{1,2} \mid s_1^2 + s_2^2 = \frac{2}{w_h}(\delta(c_J) - \lambda_0 s_5 s_6)\}. \quad (19)$$

- (ii) $\mathcal{R}_1(c_J)$ is bounded by hyperbolas in $\pi_{c_J}^{5,6}$.

The best interpretation is to visualize how the particle's energy can be given to the saddle, planar center, or vertical center projection. Let us assume that no energy is given to the center manifold, therefore allocating all possible energy in the saddle projection. This is equivalent to setting $s_1, s_2, s_3, s_4 = 0$. Then Eq (14) is transformed to $\delta(c_J) = \lambda_0 s_5 s_6$. Since c_J is fixed, the regions beyond hyperbolas $s_5 s_6 = \delta(c_J)/\lambda_0$ are energetically forbidden (see red area in Figure 5), as no more energy can be given to the saddle projection. In these hyperbolas, the corresponding 3-spheres in the center projections become a point as

$$\frac{w_h}{2}(s_1^2 + s_2^2) + \frac{w_v}{2}(s_3^2 + s_4^2) = \delta(c_J) - \lambda_0 s_5 s_6 = \delta(c_J) - \delta(c_J) = 0.$$

Therefore, in the bounding hyperbolas, the phase space can be fully determined by which (s_5, s_6) points are chosen as no energy is distributed to the center manifold.

- (iii) $\mathcal{R}_1(c_J)$ is also bounded by line segments (l_1 and l_2) in $\pi_{c_J}^{5,6}$.

The second condition $|s_5 - s_6| \leq K_{c_J}$ creates two line segments $l_2 : s_6(s_5) = s_5 - K_{c_J}$ and $l_1 : s_6(s_5) = s_5 + K_{c_J}$ such that $l_1, l_2 \in \pi_{c_J}^{5,6}$, as shown in Figure 5. These line segments and the hyperbolas presented in (ii) bound the saddle projection of $\mathcal{R}_1(c_J)$. The area to the left of l_1 corresponds to Mars' region, while the area to the right of l_2 corresponds to Phobos' region.

For each of the points in these line segments, there is a corresponding 3-sphere in $\pi_{c_J}^{1,2,3,4}$. Collectively, the family of 3-spheres generated along the line segments l_i (for $i = 1, 2$) form a 4-sphere, which we respectively denote by $S_{c_J}^4(l_i)$. This is explained by Proposition 4.1: each of the parallel line segments between l_1 and l_2 in $\pi_{c_J}^{5,6}$ correspond to a constant $s_5 - s_6 = k \in I_{c_J}$. Therefore, if the value of I_{c_J} is fixed, the remaining 5-dimensional phase space has to be homeomorphic to a 4-sphere.

When the lines l_1 and l_2 intersect the hyperbolas, the 3-spheres $S_{c_J}^3(s_5, s_6)$ reduce to points as $\delta(c_J) = \lambda_0 s_5 s_6$. On the other hand, the farther a point $(s_5, s_6) \in l_i$ lies from both hyperbolas, the larger the radius of its corresponding 3-sphere $S_{c_J}^3(s_5, s_6)$ is.

The planar case with $s_3, s_4 = 0$ offers a better visualization for the topology of these line segments. A family of 1-spheres in $\pi_{c_J}^{1,2}$, one for each point in l_1 , forms a 2-sphere $S_{c_J}^2(l_1)$ (analogous for l_2). A qualitative representation is shown in Figure 6.

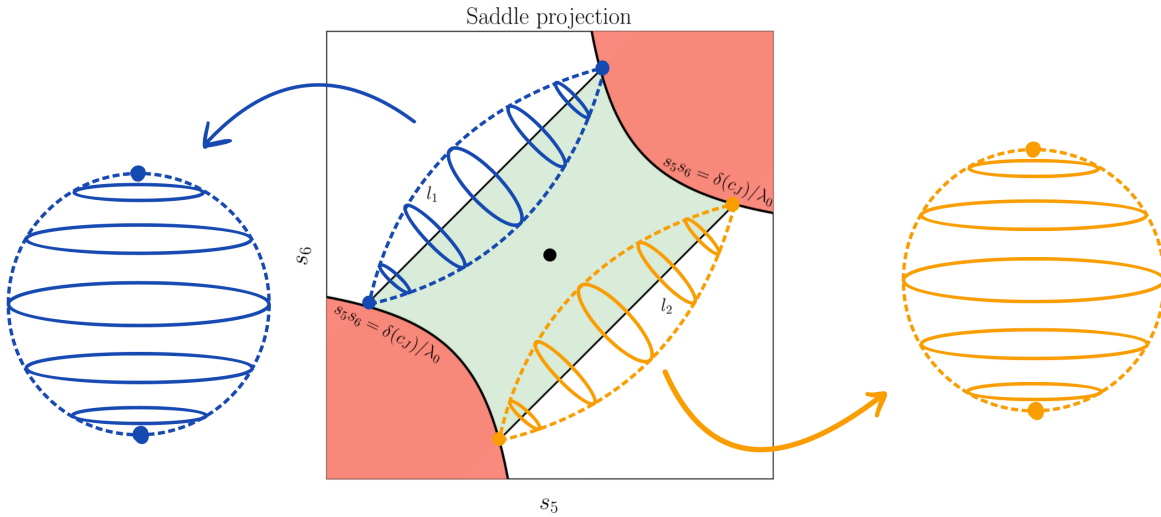


Figure 6: Formation of the 2-spheres $S_{c_J}^2(l_1)$ and $S_{c_J}^2(l_2)$ with 1-spheres $S_{c_J}^1(s_5, s_6)$ such that $(s_5, s_6) \in l_1, l_2$. The blue 1-spheres form $S_{c_J}^2(l_1)$ while the orange 1-spheres form $S_{c_J}^2(l_2)$.

- (iv) Projections of 6-dimensional orbits in $\mathcal{R}_1(c_J)$ onto $\pi_{c_J}^{5,6}$ move on branches determined by hyperbolas with $s_5 s_6 = h$, where $h \in [-\delta(c_J)/\lambda_0, \delta(c_J)/\lambda_0]$, $h \neq 0$.

As Proposition 4.2 stated, $s_5 s_6$ is a first integral. Therefore, once a trajectory is in a hyperbola determined by h , it will not leave this hyperbola inside the $\mathcal{R}_1(c_J)$. If $s_6 = 0$, the projection of the orbit in the saddle projection $\pi_{c_J}^{5,6}$ lies directly on top of the unstable manifold, meaning the trajectory will keep on distancing from the origin as $t \rightarrow \infty$. If $s_5 = 0$, the projection lies on top of the stable manifold, making the orbit go to the equilibrium point at the origin as $t \rightarrow \infty$.

After a better understanding of the linearized phase space in $\mathcal{R}_1(c_J)$, the following four types of orbits can be distinguished:

1. Periodic and quasi-periodic orbits

Let us consider $(s_5, s_6) = (0, 0)$ in the saddle-projection of the 5-dimensional energy surface $\mathcal{E}(c_J)$, the black dot in $\pi_{c_J}^{5,6}$ on Figure 5. The equivalent 3-sphere in $\pi_{c_J}^{1,2,3,4}$ for this point according to Eq (18) is:

$$S_{c_J}^3(0, 0) = \{(s_1, s_2, s_3, s_4) \in \pi_{c_J}^{1,2,3,4} \mid \frac{w_h}{2}(s_1^2 + s_2^2) + \frac{w_v}{2}(s_3^2 + s_4^2) = \delta(c_J)\}. \quad (20)$$

As $s_1^2 + s_2^2$ and $s_3^2 + s_4^2$ are first integrals, $S_{c_J}^3(0, 0)$ is invariant. Intuitively, no energy has been given to the saddle projection. All of the energy is being distributed to the center manifold, which is bounded. The 4-dimensional 3-sphere $S_{c_J}^3(0, 0)$ can be thought as a 'big 4-dimensional saddle point'. The set containing all **bounded orbits** for a fixed c_J is:

$$\mathcal{B}(c_J) = \{(s_1, \dots, s_6) \in \mathcal{R}_1(c_J) \mid (s_5, s_6) = (0, 0), (s_1, s_2, s_3, s_4) \in S_{c_J}^3(0, 0)\}.$$

These bounded orbits can be either periodic or quasi-periodic. If $s_3, s_4 = 0$, then all of the energy c_J is distributed to the planar center projection $\pi_{c_J}^{1,2}$. There exists a unique **horizontal Lyapunov orbit** \mathcal{L}_H around L_1 for a fixed c_J :

$$\mathcal{L}_H(c_J) = \{(s_1, \dots, s_6) \in \mathcal{R}_1(c_J) \mid s_1^2 + s_2^2 = 2\delta(c_J)/w_h, s_3, s_4, s_5, s_6 = 0\} \quad (21)$$

If $s_1, s_2 = 0$, then all of the energy c_J is distributed to the vertical center projection $\pi_{c_J}^{3,4}$. There exists a unique **vertical Lyapunov orbit** \mathcal{L}_V around L_1 for a fixed c_J :

$$\mathcal{L}_V(c_J) = \{(s_1, \dots, s_6) \in \mathcal{R}_1(c_J) \mid s_3^2 + s_4^2 = 2\delta(c_J)/w_v, s_1, s_2, s_5, s_6 = 0\}. \quad (22)$$

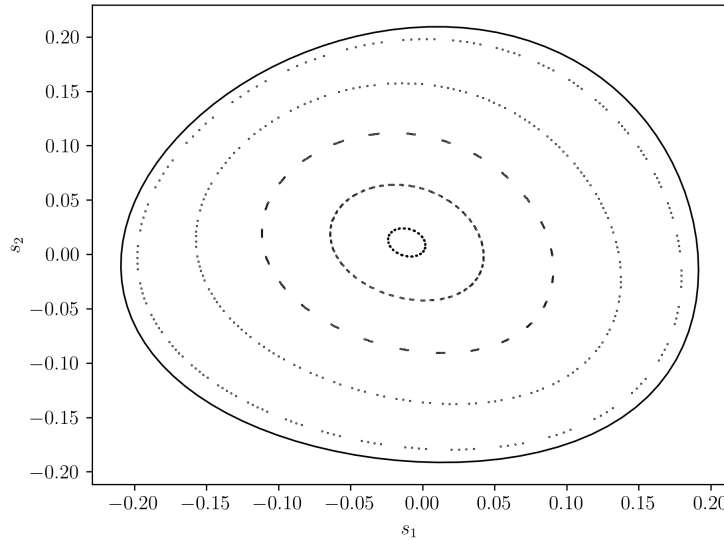


Figure 7: The solid outer line represents the unique horizontal Lyapunov orbit for $C_J = 3.000027$ in the Mars-Phobos system, denoted by $\mathcal{L}_H(3.000027)$. The dashed lines represent Lissajous orbits. This plot is known as a Poincaré section.

Remark 4.3. Let $c_J \in \mathbb{R}$ be fixed. Note that $\mathcal{L}_H(c_J)$ and $\mathcal{L}_V(c_J)$ are periodic orbits, and $\mathcal{L}_H(c_J), \mathcal{L}_V(c_J) \subset \mathcal{B}(c_J)$.

The existence and uniqueness of vertical and horizontal Lyapunov orbits is guaranteed by the Lyapunov Center Theorem in (Abraham et al. 1985). If $s_1, s_2, s_3, s_4 \neq 0$, then these orbits are considered quasi-periodic. Examples include Lissajous orbits and Quasi-halo orbits. For more information, see (Gómez, Jorba, et al. 1998) and (Gómez, Jorba, et al. 2001).

The (s_1, s_2) -space projection of $\mathcal{B}(3.000027)$ for L_1 in the Phobos-Mars system is shown in Figure 7. The solid outer line represents the horizontal Lyapunov orbit $\mathcal{L}_H(3.000027)$, and the interior dashed orbits correspond to quasi-periodic orbits known as Lissajous. Since they have some energy in the (s_3, s_4) -space too, their radius in the (s_1, s_2) -space is smaller.

2. Asymptotic orbits

These correspond to the green arrows in the saddle projection $\pi_{c_J}^{5,6}$ of Figure 5:

$$\begin{aligned}\mathcal{A}(c_J) &= \{(s_1, \dots, s_6) \in \mathcal{R}_1(c_J) \mid s_5 s_6 = 0 \ (s_5, s_6 \neq 0), \quad H_2(s_1, \dots, s_6) = \delta(c_J)\} \\ &= \{(s_1, \dots, s_6) \in \mathcal{R}_1(c_J) \mid \frac{w_h}{2}(s_1^2 + s_2^2) + \frac{w_v}{2}(s_3^2 + s_4^2) = \delta(c_J), \ s_5 s_6 = 0 \ (s_5, s_6 \neq 0)\}.\end{aligned}$$

Each of the four segments in the axes of $\pi_{c_J}^{5,6}$ that have $s_5 s_6 = 0$ (excluding point $(s_5, s_6) = (0, 0)$) correspond to 4-dimensional tubes/cylinders in $\pi_{c_J}^{1,2,3,4}$. Topologically, they are considered cylinders because their structure is $S_{c_J}^3(0, 0) \times \mathbb{R}$, as only one nonzero parameter (s_5 or $s_6 \in \mathbb{R}$) apart from $S_{c_J}^3(0, 0)$ is in the definition of $\mathcal{A}(c_J)$. These 4-dimensional tubes consist of orbits that are asymptotic to $S_{c_J}^3(0, 0)$.

Let us separate two different types of asymptotic orbits, the ones that approach $S_{c_J}^3(0, 0)$ as time increases and the ones that approach $S_{c_J}^3(0, 0)$ as time decreases. Let us start with the **local invariant stable manifold** asymptotic to $S_{c_J}^3(0, 0)$:

$$\mathcal{W}^s(P_i|S_{c_J}^3(0, 0)) = \{(s_1, \dots, s_6) \in \mathcal{A}(c_J) \mid s_5 = 0, \ s_6 \neq 0\},$$

where $P_i = \{\text{Mars, Phobos}\} = \{M, P\}$ describes the two possible options, as s_6 can be positive or negative. $\mathcal{W}^s(P_i|S_{c_J}^3(0, 0))$ is a 4-dimensional tube that asymptotically approaches the 'big saddle point' $S_{c_J}^3(0, 0)$ as time increases. In Figure 5, the green arrows approach the black dot in $\pi_{c_J}^{5,6}$. When $s_6 > 0$, $\mathcal{W}^s(M|S_{c_J}^3(0, 0))$ approaches $S_{c_J}^3(0, 0)$ from Mars' region, whereas when $s_6 < 0$, $\mathcal{W}^s(P|S_{c_J}^3(0, 0))$ approaches $S_{c_J}^3(0, 0)$ from Phobos' region.

The **local invariant unstable manifold** asymptotic to $S_{c_J}^3(0, 0)$ is:

$$\mathcal{W}^u(P_i|S_{c_J}^3(0, 0)) = \{(s_1, \dots, s_6) \in \mathcal{A}(c_J) \mid s_6 = 0, \ s_5 \neq 0\}.$$

It is analogous to the stable manifold, but instead of orbits asymptotically approaching $S_{c_J}^3(0, 0)$ as time increases, it happens when time decreases. When $s_5 > 0$, $\mathcal{W}^u(P|S_{c_J}^3(0, 0))$ evolves towards Phobos, whereas when $s_5 < 0$, $\mathcal{W}^u(M|S_{c_J}^3(0, 0))$ evolves towards Mars.

In the planar case when $s_3, s_4 = 0$, these 4-dimensional tubes reduce down to 2-dimensional tubes. Instead of being asymptotic to $S_{c_J}^3(0, 0)$, they are asymptotic to the unique horizontal Lyapunov orbit of energy c_J , denoted by $\mathcal{L}_H(c_J)$. Figure 8 shows $\mathcal{W}^s(M|\mathcal{L}_H(c_J))$ in blue and $\mathcal{W}^u(P|\mathcal{L}_H(c_J))$ in orange.

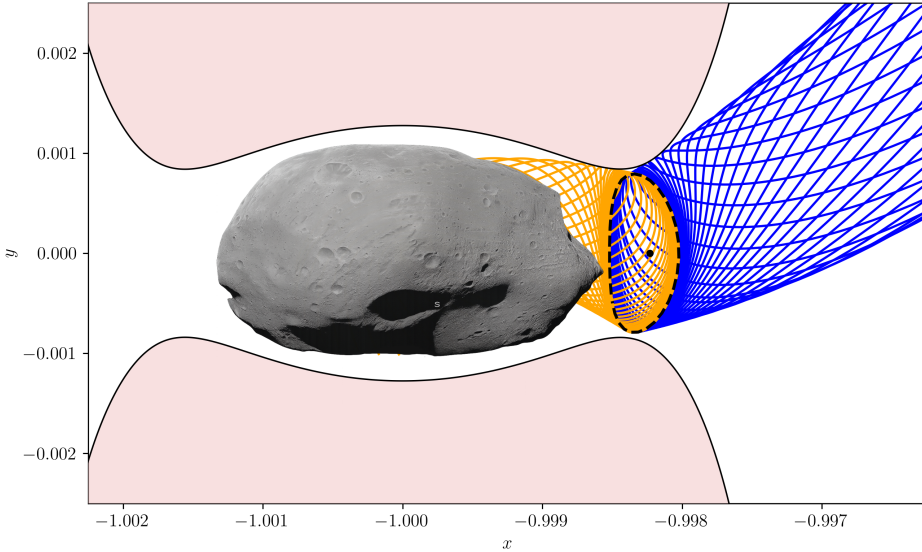


Figure 8: Invariant manifolds around L_1 for $C_J = 3.000026$. The red area represents the energetically forbidden regions, limited by the ZVC. The blue mesh consists of trajectories in the stable manifold $\mathcal{W}^s(M|\mathcal{L}_H(3.000026))$, while the orange mesh consists of trajectories in the unstable manifold $\mathcal{W}^u(P|\mathcal{L}_H(3.000026))$. At their intersection, the unique horizontal Lyapunov orbit $\mathcal{L}_H(3.000026)$ is represented with black dashed lines. The black dot represents L_1 .

3. Transit orbits

These are the orbits that project onto $\pi_{c_J}^{5,6}$ as hyperbolas that connect l_1 and l_2 , in either direction. Two examples as red arrows are plotted in Figure 5. These orbits are hyperbolic segments in $\pi_{c_J}^{5,6}$ such that $s_5 s_6 = h \in (0, \delta(c_J)/\lambda_0)$. In $\pi_{c_J}^{5,6}$, the hyperbolas that go from l_1 to l_2 travel from Mars' region to Phobos' region, while hyperbolas that go from l_2 to l_1 travel from Phobos' region to Mars' region. Equivalently, in the complete phase space of the equilibrium region $\mathcal{R}_1(c_J)$, transit orbits go from $S_{c_J}^4(l_1)$ to $S_{c_J}^4(l_2)$, and vice versa. Remember that $S_{c_J}^4(l_1)$ is the boundary between $\mathcal{R}_1(c_J)$ and Mars' region while $S_{c_J}^4(l_2)$ is the boundary between $\mathcal{R}_1(c_J)$ and Phobos' region. Since they go from one boundary of $\mathcal{R}_1(c_J)$ to the other, they are called **transit orbits**. They are mathematically defined as:

$$\mathcal{T}(c_J) = \{(s_1, \dots, s_6) \in \mathcal{R}_1(c_J) \mid s_5 s_6 \in (0, \delta(c_J)/\lambda_0), H_2(s_1, \dots, s_6) = \delta(c_J)\}.$$

Proposition 4.3 (Main Proposition). *Let $c_J \in \mathbb{R}$ be fixed. Transit orbits $\mathcal{T}(c_J)$ are contained within $\mathcal{W}^s(P_i|S_{c_J}^3(0, 0))$ and $\mathcal{W}^u(P_i|S_{c_J}^3(0, 0))$, where $P_i = \{\text{Mars, Phobos}\}$.*

Proof. Let us work with the planar CR3BP for simplification (the proof for the CR3BP is analogous). When an orbit is asymptotic to $\mathcal{L}_H(c_J)$, its projection onto $\pi_{c_J}^{5,6}$ follows the stable or unstable branch/axis of $\pi_{c_J}^{5,6}$ (green arrows) as $s_5 s_6 = 0$ is true for all asymptotic orbits. Without loss of generality, let us assume that $s_5 = 0, s_6 > 0$. For every point $(0, s_6)$, there is a corresponding 1-sphere in $\pi_{c_J}^{1,2}$ with radius $\sqrt{2\delta(c_J)/w_h}$ (see Eq (19)). However, if a transit orbit is chosen so that $s_5 s_6 = h \in (0, \delta(c_J))$, then for each point (s_5, s_6) in the projection of the transit orbit onto $\pi_{c_J}^{5,6}$, there is a 1-sphere in $\pi_{c_J}^{1,2}$ with radius $\sqrt{2(\delta(c_J) - \lambda_0 s_5 s_6)/w_h}$. As $s_5 s_6 > 0$, the projection of the transit orbit onto $\pi_{c_J}^{1,2}$ clearly has a smaller radius than the one corresponding to any asymptotic orbit with $s_5 s_6 = 0$. \square

Remark 4.4. Note that in the proof of the Main Proposition, the fact that $\mathcal{W}^s(P_i|S_{c_J}^3(0, 0))$, $\mathcal{W}^u(P_i|S_{c_J}^3(0, 0)) \subset \mathcal{A}(c_J)$ is important. Specifically, for a fixed $c_J \in \mathbb{R}$, the following is true:

$$\mathcal{A}(c_J) = \mathcal{W}^s(M|S_{c_J}^3(0, 0)) \cup \mathcal{W}^s(P|S_{c_J}^3(0, 0)) \cup \mathcal{W}^u(M|S_{c_J}^3(0, 0)) \cup \mathcal{W}^u(P|S_{c_J}^3(0, 0)).$$

In the planar CR3BP, the transit orbits that go from Mars' region to Phobos' region travel from $S_{c_J}^2(l_1)$ to $S_{c_J}^2(l_2)$, meaning they have to go through $\text{int}(\mathcal{W}^s(M|\mathcal{L}_H(c_J)))$ first, then $\text{int}(\mathcal{L}_H(c_J))$ and finally $\text{int}(\mathcal{W}^u(P|\mathcal{L}_H(c_J)))$. In Figure 8, transit orbits first travel inside the blue tube before entering the orange tube on their way to impacting Phobos.

4. Non-transit orbits

Instead of traveling from $S_{c_J}^4(l_1)$ to $S_{c_J}^4(l_2)$ or vice versa, these orbits go from one hemisphere of $S_{c_J}^4(l_i)$ to the other hemisphere of the same 4-sphere (for $i = 1, 2$).

Non-transit orbits are represented as blue arrows in Figure 5 and are defined as:

$$\mathcal{N}(c_J) = \{(s_1, \dots, s_6) \in \mathcal{R}_1(c_J) \mid s_5 s_6 \in (-\delta(c_J)/\lambda, 0), H_2(s_1, \dots, s_6) = \delta(c_J)\}.$$

Therefore, they do not transit from Mars' region to Phobos' region. If a non-transit orbit is chosen so that $s_5 s_6 = h \in (-\delta(c_J), 0)$, then for each point (s_5, s_6) in the projection of this non-transit orbit onto $\pi_{c_J}^{5,6}$, there is a 1-sphere in $\pi_{c_J}^{1,2}$ with radius $\sqrt{2(\delta(c_J) - \lambda_0 s_5 s_6)/w_h}$. Since in this case $s_5 s_6 < 0$, the radius is bigger than the one corresponding to any asymptotic orbit with $s_5 s_6 = 0$. As a result, orbits outside of the invariant manifolds are non-transit. In Figure 8, non-transit orbits would travel outside of the 2-dimensional blue and orange tubes, and would be blocked by the ZVC.

In conclusion: there is a way to determine transit and non-transit orbits. Asymptotic orbits $\mathcal{A}(c_J)$ forming the stable and unstable manifolds of $S_{c_J}^3(0, 0)$ separate them. The orbits inside these 4-dimensional tubes are transit orbits $\mathcal{T}(c_J)$ while the orbits outside these tubes are non-transit orbits $\mathcal{N}(c_J)$.

5 The parameterization method

In the planar CR3BP, finding horizontal Lyapunov orbits around L_1 and their associated manifolds is crucial for determining the transit orbits of dust particles that impact Phobos. The parameterization method is a semi-analytical method that provides parameterizations for invariant manifolds around fixed points using power series expansions. The following explanation of the parameterization method has been inspired by Chapter 2.2 in (Haro et al. 2016), and adapted to our case.

Let us recover $\dot{X} = F(X)$ from past sections in reference frame \mathfrak{R}_n , with $X = (x, p_x, y, p_y, z, p_z)$, F the vector field associated with the CR3BP, and $X_0 = 0$ being L_1 in \mathfrak{R}_n . In addition, let us remember that $A = DF(0)$ is the Jacobian matrix of F at L_1 , and that it is the matrix that governs the linearized system $\dot{X} = AX$. Also, remember that $E_A = E^s \cup E^u \cup E^c$ is the set containing all eigenvectors of A , where u_λ is the eigenvector of eigenvalue λ .

5.1 The invariance equation and the cohomological equations

Suppose we select $1 \leq d \leq 6$ eigenvectors from E_A . Let $P_T \in \mathbb{C}^{6 \times d}$ be a matrix containing these selected eigenvectors as its columns and E^d the d -dimensional subspace spanned by these columns. Since E^d has to be invariant for A for the parameterization method to work, E^d can only be equal to E^s , E^u or E^c . With the parameterization method, a higher order approximation W of the invariant manifold \mathcal{W} tangent to E^d at L_1 is calculated.

The parameterization we are interested in can be described by $X = W(s)$, with $s = (s_{i_1}, \dots, s_{i_d}) \in \mathfrak{R}_l$ acting as the coordinates of our invariant manifold such that $W(0) = 0$, where $\{i_1, \dots, i_d\} \in \{1, 2, 3, 4, 5, 6\}$. The parameterization method also provides a reduced vector field $\dot{s} = f(s)$, which describes the dynamics of the invariant manifold \mathcal{W} such that $f(0) = 0$.

Now, let us consider $P \in \mathbb{C}^{6 \times 6}$, the matrix containing all of the eigenvectors in E_A as its columns. Essentially, P is a change of base matrix from \mathfrak{R}_l to \mathfrak{R}_n such that:

$$P^{-1}AP = \Lambda = \begin{pmatrix} \Lambda_T & 0 \\ 0 & \Lambda_N \end{pmatrix}, \quad (23)$$

where $\Lambda_T \in \mathbb{C}^{d \times d}$ is a diagonal matrix with the associated eigenvalues of eigenspace E^d , and $\Lambda_N \in \mathbb{C}^{(6-d) \times (6-d)}$ is a diagonal matrix with the associated eigenvalues of eigenspace $E_A \setminus E_d$. Note that Λ is diagonal because E_A is the eigenbasis for \mathfrak{R}_l . The first order approximation of \mathcal{W} is given by $W_1(s) = P_T s$, and the first order approximation of f is given by $f_1(s) = \Lambda_T s$.

For higher order terms, $X = W(s)$ is substituted into $\dot{X} = F(X)$, which results in $DW(s)\dot{s} = F(W(s))$. If $\dot{s} = f(s)$ is used, the commonly known ***invariance equation*** is obtained:

$$DW(s)f(s) = F(W(s)). \quad (24)$$

Before solving the invariance equation, let the following functions be expanded as a power series around L_1 of the Mars-Phobos system:

$$f(s) = \Lambda_T s + \sum_{k>1} f_k(s), \quad W(s) = P_T s + \sum_{k>1} W_k(s), \quad F(X) = AX + \sum_{k>1} F_k(X), \quad (25)$$

where the linear terms have already been calculated, and subindex k represents terms of k in the expansion.

To solve the invariance equation, we recursively compute W order by order for $k > 1$. Specifically, to calculate terms of order k , we assume that lower order terms, $W_{<k}$ and $f_{<k}$, have been calculated.

The **cohomological equations** of order k calculate W_k and f_k . While the complete procedure for deriving them from the invariance equation is detailed in (Haro et al. 2016), this thesis only presents the essential components to solve and implement them in our case:

- Known lower-term contribution:

$$C_k(s) = [F(W_{<k}(s))]_k - [DW_{<k}(s)f_{<k}(s)]_k,$$

where the first summand represents the homogeneous terms of degree k of $F(W_{<k}(s))$ and the second summand represents the homogeneous terms of degree k of $DW_{<k}(s)f_{<k}(s)$. The term C_k is obtained from previous iterations. Let us define $\eta_k(s) = -P^{-1}C_k(s)$.

- Unknowns to be solved at order k :

Let us define $\xi_k(s) = P^{-1}W_k(s)$. Since the cohomological equations can be divided between the tangent equations to E^d and the normal equations to E^d , the following are defined:

$$\begin{aligned}\xi_k^T(s) &= (I_d \quad 0)\xi_k(s), & \xi_k^N(s) &= (0 \quad I_{6-d})\xi_k(s), \\ \eta_k^T(s) &= (I_d \quad 0)\eta_k(s), & \eta_k^N(s) &= (0 \quad I_{6-d})\eta_k(s).\end{aligned}$$

Then, the **tangent cohomological equation of order k** is (Haro et al. 2016):

$$\Lambda_T \xi_k^T(s) - D\xi_k^T(s)\Lambda_T s - f_k(s) = \eta_k^T(s), \quad (26)$$

and the **normal cohomological equation of order k** is (Haro et al. 2016):

$$\Lambda_N \xi_k^N(s) - D\xi_k^N(s)\Lambda_N s = \eta_k^N(s). \quad (27)$$

5.2 Solving the cohomological equations

Let us denote the components of vectors $\xi_k(s)$, $\eta_k(s)$ and $f_k(s)$:

$$\xi_k(s) = (\xi_k^{i_1}(s), \dots, \xi_k^{i_6}(s)), \quad \eta_k(s) = (\eta_k^{i_1}(s), \dots, \eta_k^{i_6}(s)), \quad f_k(s) = (f_k^{i_1}(s), \dots, f_k^{i_6}(s)),$$

where each component is a homogeneous polynomial of degree k with the following form:

$$\xi_k^j(s) = \sum_m \xi_m^j s_{i_1}^{m_1} s_{i_2}^{m_2} \cdots s_{i_d}^{m_d}, \quad \eta_k^j(s) = \sum_m \eta_m^j s_{i_1}^{m_1} s_{i_2}^{m_2} \cdots s_{i_d}^{m_d}, \quad f_k^j(s) = \sum_m f_m^j s_{i_1}^{m_1} s_{i_2}^{m_2} \cdots s_{i_d}^{m_d},$$

where $m = (m_1, \dots, m_d)$ is a vector representing the exponents of each parameter in s and $\sum m_i = k$. In other words, (m_1, \dots, m_d) is associated with the monomial $s_{i_1}^{m_1} s_{i_2}^{m_2} \cdots s_{i_d}^{m_d}$. Since Λ is a diagonal matrix, the diagonal entries for Λ_T are $\lambda_{i_1}, \dots, \lambda_{i_d}$ (eigenvalues from the eigenvectors in E^d), and the diagonal entries for Λ_N are $\lambda_{i_{d+1}}, \dots, \lambda_{i_6}$, (eigenvalues from the eigenvectors in $E_A \setminus E^d$). Expressing Eq (27) for $j = i_{d+1}, \dots, i_6$:

$$\lambda_j \xi_k^j(s) - D\xi_k^j(s)(\lambda_{i_1} s_{i_1}, \dots, \lambda_{i_d} s_{i_d})^t = \eta_k^j(s) \implies (\lambda_j - \lambda_T m) \xi_m^j = \eta_m^j,$$

where $\lambda_T m = \lambda_{i_1} m_1 + \lambda_{i_2} m_2 + \dots + \lambda_{i_d} m_d$, and the second equation has been obtained after comparing coefficients ξ_m^j and η_m^j one by one for every possible value of m . This is possible due to the choice of matrix P and the diagonalization of A . Therefore, the final result for $j = i_{d+1}, \dots, i_6$ is:

$$\xi_m^j = \frac{\eta_m^j}{\lambda_j - \lambda_T m} \quad (28)$$

For the CR3BP, $\lambda_i = \lambda_T m$ is a possibility and a proper examination of the eigenvalues is needed. However, for the Mars-Phobos system, the eigenvalues do not make the power series diverge. The remaining solutions for $j = i_1, \dots, i_d$ can be found through Eq (26) by setting $f_m^j = 0$ for $j = i_1, \dots, i_d$. This transforms Eq (26) into Eq (27) and as a result Eq (28) can also be used for $j = i_1, \dots, i_d$. For information about the different ways and styles to solve the cohomological equations when $\lambda_j = \lambda_L m$, see Chapter 2.2.3 in (Haro et al. 2016).

Finally, the term of order k of the power series $W(s)$ is:

$$W_k^j(s) = P \xi_k^j(s), \quad (29)$$

for $j = i_1, \dots, i_6$.

5.3 Application of the parameterization method

This section focuses on applying the parameterization method to calculate the second-order parameterization of \mathcal{L}_H . The aim is to provide a specific example of the parameterization method in a simplified setting. Since this example is restricted to the planar CR3BP where $z, \dot{z} = 0$, the corresponding total phase space is 4-dimensional rather than 6-dimensional.

The calculation is organized into the following steps:

I. Calculate P and P_T

Since we are in the planar case, we consider the 4-dimensional eigenvectors $v_{\lambda_0}, v_{-\lambda_0}, v_{w_h i}$ and $v_{-w_h i}$ of the top left 4×4 submatrix of A (specific expressions for the eigenvectors are shown in Appendix 9.1). Then P can be written as:

$$P = (v_{w_h i}, v_{-w_h i}, v_{\lambda_0}, v_{-\lambda_0}) = \begin{pmatrix} p_{11} & -p_{11} & p_{13} & -p_{13} \\ p_{21} & p_{21} & p_{23} & p_{23} \\ p_{31} & p_{31} & p_{33} & p_{33} \\ p_{41} & -p_{41} & p_{43} & -p_{43} \end{pmatrix},$$

where different eigenvectors have similar structures (this symmetry is explained in Appendix 9.1 through the expression of eigenvectors v_λ). Also, note that $P_T = (v_{w_h i}, v_{-w_h i})$ consists of the first two columns of P and $s = (s_1, s_2)^t$.

II. First-order approximation of \mathcal{L}_H

With P and P_T , the following is computed:

$$W_1(s) = P_T s, \quad \Lambda = P^{-1} A P, \quad f_1(s) = \Lambda_T s.$$

First, the first order approximation of \mathcal{L}_H is:

$$W_1(s_1, s_2) = P_T(s_3, s_4)^t = (p_{11}(s_1 - s_2), p_{21}(s_1 + s_2), p_{31}(s_1 + s_2), p_{41}(s_1 - s_2))^t.$$

The eigenvalues form the following diagonal matrix Λ :

$$\Lambda = \begin{pmatrix} w_h i & 0 & 0 & 0 \\ 0 & -w_h i & 0 & 0 \\ 0 & 0 & \lambda_0 & 0 \\ 0 & 0 & 0 & -\lambda_0 \end{pmatrix}.$$

Consequently, the first order approximation of the reduced field f is:

$$f_1(s_1, s_2) = \Lambda_T(s_1, s_2)^t = (w_h s_1 i, -w_h s_2 i)^t.$$

III. Computation of $C_2(s)$

In this case, $C_2(s) = [F(W_{<2}(s))]_2 - [DW_{<2}(s)f_{<2}(s)]_2$. Let us calculate both summands:

$$\begin{aligned} F(W_{<2}(s)) = F(W_1(s)) &\implies [F(W_{<2}(s))]_2 = F_2(W_1(s)), \\ DW_{<2}(s)f_{<2}(s) = DW_1(s)f_1(s) &\implies [DW_{<2}(s)f_{<2}(s)]_2 = 0. \end{aligned}$$

Since $[\cdot]_2$ extracts only the second-order terms, we obtain $C_2(s) = F_2(W_1(s))$. Using the expression for F_2 in Appendix 9.2, we obtain:

$$C_2(s_1, s_2) = (0, \frac{3}{2}c_3((2p_{11}^2 - p_{31}^2)s_1^2 - (4p_{11}^2 + 2p_{31}^2)s_1s_2 + (2p_{11}^2 - p_{31}^2)s_2^2), 0, -3c_3p_{11}p_{31}(s_1^2 - s_2^2))^t,$$

where c_3 is a coefficient derived in Appendix 9.1.

IV. Final formulas

$$\eta_2(s) = -P^{-1}C_2(s), \quad \xi_m^j(s) = \frac{\eta_m^j(s)}{\lambda_j - m\lambda_T}, \quad W_2(s) = P\xi_2(s).$$

Since P is a square matrix formed by 4 different eigenvectors which are linearly independent, P has full rank 4 and is invertible. Let $Q = P^{-1}$:

$$Q = \begin{pmatrix} q_{11} & q_{12} & q_{13} & q_{14} \\ q_{21} & q_{22} & q_{23} & q_{24} \\ q_{31} & q_{32} & q_{33} & q_{34} \\ q_{41} & q_{42} & q_{43} & q_{44} \end{pmatrix} = \begin{pmatrix} q_{11} & q_{12} & q_{13} & q_{14} \\ -q_{11} & q_{12} & q_{13} & -q_{14} \\ q_{31} & q_{32} & q_{33} & q_{34} \\ -q_{31} & q_{32} & q_{33} & -q_{34} \end{pmatrix}.$$

As it can be seen with matrix P , its inverse Q can be written using only 8 values as the second and fourth row can be expressed with values from the first and third row. The next step in the procedure is:

$$\eta_2(s_1, s_2) = -QC_2(s_1, s_2) = \begin{pmatrix} \alpha_{(2,0)}^1 s_1^2 + \alpha_{(1,1)}^1 s_1 s_2 + \alpha_{(2,0)}^2 s_2^2 \\ \alpha_{(2,0)}^2 s_1^2 + \alpha_{(1,1)}^1 s_1 s_2 + \alpha_{(2,0)}^1 s_2^2 \\ \alpha_{(2,0)}^3 s_1^2 + \alpha_{(1,1)}^3 s_1 s_2 + \alpha_{(2,0)}^4 s_2^2 \\ \alpha_{(2,0)}^4 s_1^2 + \alpha_{(1,1)}^3 s_1 s_2 + \alpha_{(2,0)}^3 s_2^2 \end{pmatrix},$$

where:

$$\alpha_{(1,1)}^i = 3c_3q_{i2}(2p_{11}^2 + p_{31}^2) \quad i = 1, 3 \quad (30)$$

$$\alpha_{(2,0)}^i = -3c_3 \begin{cases} \frac{1}{2}q_{12}(2p_{11}^2 - p_{31}^2) + (-1)^i q_{14}p_{11}p_{31} & i = 1, 2 \\ \frac{1}{2}q_{32}(2p_{11}^2 - p_{31}^2) + (-1)^i q_{34}p_{11}p_{31} & i = 3, 4 \end{cases} \quad (31)$$

The twelve possible coefficients for η_2 can be expressed with just six coefficients shown in Eqs (30),(31). These coefficients only depend on matrices P, Q and c_3 . The next step is described by the following equation:

$$\xi_m^j(s_1, s_2) = \frac{\eta_m^i(s_1, s_2)}{\lambda_j - m\lambda_T},$$

where $m = (m_1, m_2)$ and $m_1, m_2 \in \{0, 1, 2\}$ represent the value of the exponents of s_1, s_2 . Additionally, $m\lambda_T = w_h(m_1 - m_2)i$. Computing all of the values we get:

$$\xi_2(s_1, s_2) = \begin{pmatrix} \xi_{(2,0)}^1 s_1^2 + \xi_{(1,1)}^1 s_1 s_2 + \xi_{(0,2)}^1 s_2^2 \\ \xi_{(2,0)}^2 s_1^2 + \xi_{(1,1)}^2 s_1 s_2 + \xi_{(0,2)}^2 s_2^2 \\ \xi_{(2,0)}^3 s_1^2 + \xi_{(1,1)}^3 s_1 s_2 + \xi_{(0,2)}^3 s_2^2 \\ \xi_{(2,0)}^4 s_1^2 + \xi_{(1,1)}^4 s_1 s_2 + \xi_{(0,2)}^4 s_2^2 \end{pmatrix} = \begin{pmatrix} \frac{\alpha_{(2,0)}^1}{\lambda_0 - 2w_h i} s_1^2 + \frac{\alpha_{(1,1)}^1}{\lambda_0} s_1 s_2 + \frac{\alpha_{(2,0)}^2}{\lambda_0 + 2w_h i} s_2^2 \\ -\frac{\alpha_{(2,0)}^2}{\lambda_0 + 2w_h i} s_1^2 - \frac{\alpha_{(1,1)}^1}{\lambda_0} s_1 s_2 + \frac{\alpha_{(2,0)}^1}{-\lambda_0 + 2w_h i} s_2^2 \\ -\frac{\alpha_{(2,0)}^3}{w_h i} s_1^2 + \frac{\alpha_{(1,1)}^3}{w_h i} s_1 s_2 + \frac{\alpha_{(2,0)}^4}{3w_h i} s_2^2 \\ -\frac{\alpha_{(2,0)}^4}{3w_h i} s_1^2 - \frac{\alpha_{(1,1)}^3}{w_h i} s_1 s_2 + \frac{\alpha_{(2,0)}^3}{w_h i} s_2^2 \end{pmatrix},$$

where $\xi_2(s_1, s_2) = (\xi_2^1(s_1, s_2), \xi_2^2(s_1, s_2), \xi_2^3(s_1, s_2), \xi_2^4(s_1, s_2))^t$ has been calculated. Finally, the second-order terms of \mathcal{L}_H are:

$$W_2(s_1, s_2) = P\xi_2(s_1, s_2) = \begin{pmatrix} \sum_{j=1}^4 p_{1j} \xi_2^j(s_1, s_2) \\ \sum_{j=1}^4 p_{2j} \xi_2^j(s_1, s_2) \\ \sum_{j=1}^4 p_{3j} \xi_2^j(s_1, s_2) \\ \sum_{j=1}^4 p_{4j} \xi_2^j(s_1, s_2) \end{pmatrix}.$$

6 Methodology

This section first explains how the parameterization of invariant manifolds in \mathcal{R}_1 is computed. Then, the numerical integration of trajectories is discussed and finally, the method for finding planar transit orbits is presented.

6.1 Computation of the parameterization of invariant manifolds

The calculation of a higher order power series for the stable, unstable and center manifolds through the parameterization method is out of the scope of this thesis. As seen in Section 5.3, the second-order terms of a horizontal Lyapunov orbit already imply significant calculation difficulties. Therefore, my supervisor facilitated a Python code² that uses the parameterization method to calculate the invariant manifolds in \mathcal{R}_1 up to order 15.

Equivalently, this code allows for the transformation of coordinates from \mathfrak{R}_l to \mathfrak{R}_n . Given an input in the form of $(s_1, s_2, s_3, s_4, s_5, s_6)$, it returns $(x, y, z, \dot{x}, \dot{y}, \dot{z})$. Note that this code is only functional for orbits in the equilibrium region of L_1 . Outside of \mathcal{R}_1 , the parameterization method stops providing a good approximation of the invariant manifolds. As a result, interchanging coordinates between $(x, y, z, \dot{x}, \dot{y}, \dot{z})$ and $(s_1, s_2, s_3, s_4, s_5, s_6)$ is crucial. Coordinates in \mathfrak{R}_l are used to calculate bounded orbits in \mathcal{R}_1 , and then their corresponding coordinates in \mathfrak{R}_n are used to integrate Eq (2) backward and forward in time outside of \mathcal{R}_1 .

6.2 Numerical integration of trajectories

To find how the invariant manifolds act outside \mathcal{R}_1 , initial conditions inside \mathcal{R}_1 are numerically integrated with the differential equations of the CR3BP through Eq (2) into Mars' region or Phobos' region. With initial conditions $(x_0, y_0, z_0, \dot{x}_0, \dot{y}_0, \dot{z}_0) \in \mathcal{R}_1$ at $t_0 = 0$ and $[0, t_f]$ as the integration time interval, the `solve_ivp` function from Python library `scipy.integrate` with integration method RK-45 returns $(x(t_i), y(t_i), z(t_i), \dot{x}(t_i), \dot{y}(t_i), \dot{z}(t_i))$ for several $t_i \in [t_0, t_f]$. Note that t_f can either be positive or negative, as stable manifolds are integrated backward in time and unstable manifolds forward in time.

6.3 Determination of planar transit orbits

Since this method details how to obtain planar transit orbits, it assumes $z, \dot{z} = 0$ and $s_3, s_4 = 0$. Accordingly, all of the notation introduced in Section 4.2 regarding phase space topology is adapted to the 4-dimensional planar phase-space. Throughout this section, as well as in Section 7, we adopt notation $(s_1, s_2, s_5, s_6) \in \mathcal{R}_1$ and $(x, y, \dot{x}, \dot{y}) \in \mathbb{R}^4$. Lastly, in the remaining sections, we interpret $\mathcal{T}(c_J)$ exclusively as the set of transit orbits traveling from Mars' region to Phobos' region, disregarding those that travel from Phobos' region to Mars' region.

Since the set of transit orbits $\mathcal{T}(c_J)$ depends on the energy of the test particle c_J , the determination of planar transit orbits is performed for different energies:

$$\mathcal{C} = [3.000024, 3.000025, 3.000026, 3.000027, 3.0000275, 3.000028].$$

Note that for Jacobi constants higher than $C_J = 3.00002815$, the ZVC separate Mars' region and Phobos's region, implying that $\mathcal{T}(C_J > 3.00002815) = \emptyset$. See Figure 4 for visual support.

²Power series expansions are originally calculated with C++ by Ruilong Li.

Since there is still no observational data specific to the amount of dust particles around Mars' region, we assume that the density of dust particles is uniform across all energy levels.

The general process begins by computing the horizontal Lyapunov orbit for a fixed energy $\mathcal{L}_H(c_J)$. Next, its associated stable manifold branch that enters Mars' region is calculated, denoted by $\mathcal{W}^s(M|\mathcal{L}_H(c_J))$. Then, a set of the orbits inside $\mathcal{W}^s(M|\mathcal{L}_H(c_J))$ at section $y = 0.04$ is selected, which provide initial conditions of transit orbits. These initial conditions are then integrated forward in time until they impact Phobos. The following four subsections explain this process step by step:

I. Determination of the unique horizontal Lyapunov orbit

First, the unique horizontal Lyapunov orbit for each energy in \mathcal{C} must be calculated. Let $c_J \in \mathcal{C}$ be fixed. Since the goal is to compute $\mathcal{L}_H(c_J)$, we set $s_5, s_6 = 0$. The next step is to find the set of coordinates $(s_1, s_2) \in \pi_{c_J}^{1,2}$ such that $(s_1, s_2, 0, 0) \in \mathcal{L}_H(c_J)$. To do so, s_2 is set to 0 and the energy constraint is used to calculate the value of $s_1 = s_1^*$ such that $s^* = (s_1^*, 0, 0, 0) \in \mathcal{L}_H(c_J)$. In other words, the equation $C_J(s^*) = c_J$ is solved numerically to find s_1^* . Once one point in the 4-dimensional phase space is in $\mathcal{L}_H(c_J)$, it can be numerically integrated until it reveals the full $\mathcal{L}_H(c_J)$. This process works because $\mathcal{L}_H(c_J)$ is a periodic orbit, and the trajectory with $s^* \in \mathcal{L}_H(c_J)$ as its initial condition theoretically stays in $\mathcal{L}_H(c_J)$ ³.

II. Determination of the stable manifold of the horizontal Lyapunov orbit

The next step is to find $\mathcal{W}^s(M|\mathcal{L}_H(c_J))$. To do so, $s_6 \neq 0$ must be added to coordinates $(s_1, s_2, 0, 0) \in \mathcal{L}_H(c_J)$. After review, $s_6 = 0.0001$ is an optimal value for computation. Then, if points of the form $(s_1, s_2, 0, 0.0001) \in \mathcal{R}_1(c_J)$ are numerically integrated backward in time, the asymptotic orbits forming $\mathcal{W}^s(M|\mathcal{L}_H(c_J))$ are obtained. Intuitively, these orbits correspond to the blue lines in Figure 8 (for $c_J = 3.000026$). Their numerical integration is performed until section $y = 0.04$, which is outside of $\mathcal{R}_1(c_J)$ and inside Mars' region. Let $g_1(y) = y - 0.04$ and $\Sigma = \{(x, y, \dot{x}, \dot{y}) \in \mathbb{R}^4 \mid g_1(y) = 0\}$. Then $\Gamma(c_J)$ is defined as:

$$\Gamma(c_J) \equiv \mathcal{W}^s(M|\mathcal{L}_H(c_J)) \cap \Sigma = \{(x, y, \dot{x}, \dot{y}) \in \mathcal{W}^s(M|\mathcal{L}_H(c_J)) \mid g_1(y) = 0\}.$$

III. Determination of initial conditions of transit orbits

As Section 4.2 detailed, planar transit orbits are confined within 2-dimensional tubes such as $\mathcal{W}^s(M|\mathcal{L}_H(c_J))$. Consequently, initial conditions of transit orbits traveling from Mars' region to Phobos' region should be inside of $\Gamma(c_J)$:

$$\mathcal{T}(c_J)|_\Sigma = \mathcal{T}(c_J) \cap \Sigma = \text{int}(\Gamma(c_J)) = \{(x_\Sigma, 0.04, \dot{x}_\Sigma, \dot{y}_\Sigma) \in \text{int}(\mathcal{W}^s(M|\mathcal{L}_H(c_J)))\}.$$

Note that $\Gamma(c_J)$ is the boundary of $\mathcal{T}(c_J)|_\Sigma$, and from now on will be denoted by $\partial\mathcal{T}(c_J)|_\Sigma \equiv \Gamma(c_J)$. As a result, $\mathcal{T}(c_J)|_\Sigma$ is the set of initial conditions of transit orbits at section Σ and $\partial\mathcal{T}(c_J)|_\Sigma$ is the set of initial conditions of asymptotic orbits at section Σ (the same asymptotic orbits that form $\mathcal{W}^s(M|\mathcal{L}_H(c_J))$).

The projection of $\partial\mathcal{T}(c_J)|_\Sigma$ onto the (x, \dot{x}) -space forms a closed curve homeomorphic to a 1-sphere. Therefore, the coordinates $(x_\mathcal{T}, \dot{x}_\mathcal{T})$ inside this closed curve correspond to initial conditions of transit orbits at Σ . $(x_\mathcal{T}, \dot{x}_\mathcal{T})$ are numerically stored. Since $y = 0.04$ is fixed, $C_J((x_\mathcal{T}, 0.04, \dot{x}_\mathcal{T}, \dot{y}_\mathcal{T})) = c_J$ is used to find the missing coordinate $\dot{y}_\mathcal{T}$. Consequently, 5000 points of the form $(x_\mathcal{T}, 0.04, \dot{x}_\mathcal{T}, \dot{y}_\mathcal{T})$ are calculated for each $c_J \in \mathcal{C}$, numerically obtaining $\mathcal{T}(c_J)|_\Sigma$ for each $c_J \in \mathcal{C}$.

³ $s_1^2 + s_2^2$ is a first integral of Eq (12).

IV. Transit orbits and impact statistics

Initial conditions $\mathcal{T}(c_J)|_{\Sigma}$ are integrated forward in time. They are theoretically expected to travel inside $\mathcal{W}^s(M|\mathcal{L}_H(c_J))$, then go through $\mathcal{L}_H(c_J)$, and finally travel inside $\mathcal{W}^u(P|\mathcal{L}_H(c_J))$ before ultimately impacting Phobos.

Phobos is modeled as a triaxial ellipsoid in this work, with semi-axes $a = 0.00139$, $b = 0.00122$ and $c = 0.00098$, and center coordinates in $(\mu - 1, 0, 0)$. After numerically integrating the initial conditions $\mathcal{T}(c_J)|_{\Sigma}$, the impact positions and associated velocities are stored. The set of impact states is mathematically defined as:

$$\mathcal{I}(c_J) = \{(x, y, \dot{x}, \dot{y}) \in \mathcal{T}(c_J) \mid \left(\frac{x - (\mu - 1)}{a}\right)^2 + \left(\frac{y}{b}\right)^2 - 1 = 0\}.$$

7 Results

Section 7.1 presents $\mathcal{L}_H(c_J)$ and $\partial\mathcal{T}(c_J)|_{\Sigma}$ for $c_J \in \mathcal{C}$. In Section 7.2, the initial conditions of the planar transit orbits at Σ , $\mathcal{T}(c_J)|_{\Sigma}$, are integrated forward in time to numerically show that they all hit Phobos, and to analyze their impact positions on Phobos. The impact dynamics are first analyzed for $c_J = 3.000027$, and then for $c_J \in \mathcal{C}$ to understand the energy dependence of $\mathcal{I}(c_J)$. Note that Appendix 9.3 provides an analysis of impact velocities.

7.1 Horizontal Lyapunov orbits and their stable manifolds

Figure 9 shows the family of energy-dependent horizontal Lyapunov orbits around L_1 , denoted $\mathcal{L}_H(c_J)$ for $c_J \in \mathcal{C}$. In these orbits, all of the energy c_J is confined to the (s_1, s_2) -space. As the Jacobi constant c_J approaches $C_J(L_1) \approx 3.0000281$, its corresponding Lyapunov orbits $\mathcal{L}_H(c_J)$ become more circular. This is because near L_1 , the motion is well approximated by the linearized dynamics within the equilibrium region $\mathcal{R}_1(c_J)$. However, as the horizontal Lyapunov orbits extend farther from L_1 , nonlinear effects of the CR3BP become more significant. Moreover, Figure 9 also shows how a lower c_J corresponds to a $\mathcal{L}_H(c_J)$ with a larger radius in the (s_1, s_2) -space, just as Eq (22) predicted.

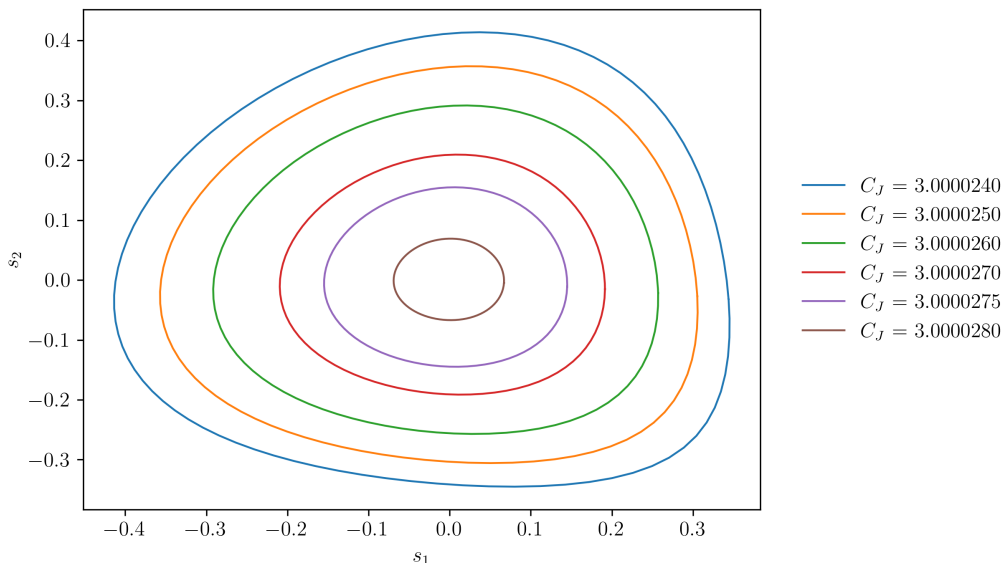


Figure 9: Horizontal Lyapunov orbits $\mathcal{L}_H(c_J)$ around the L_1 Mars-Phobos equilibrium point for all $c_J \in \mathcal{C}$. L_1 has coordinates $(s_1, s_2) = (0, 0)$.

The (x, \dot{x}) projections of $\partial\mathcal{T}(c_J)|_\Sigma$ for each $c_J \in \mathcal{C}$ are shown in Figure 10. The general topological structure of the stable manifold $\mathcal{W}^s(M|\mathcal{L}_H(c_J))$ is preserved at section $y = 0.04$, as the resulting closed curves $\partial\mathcal{T}(c_J)|_\Sigma$ are homeomorphic to the original horizontal Lyapunov orbits $\mathcal{L}_H(c_J)$. Consequently, Figure 10 numerically shows that $\mathcal{W}^s(M|\mathcal{L}_H(c_J))$ is a 2-dimensional tube that transports $L_H(c_J)$ from $\mathcal{R}_1(c_J)$ through Mars' region until section Σ for $c_J \in \mathcal{C}$.

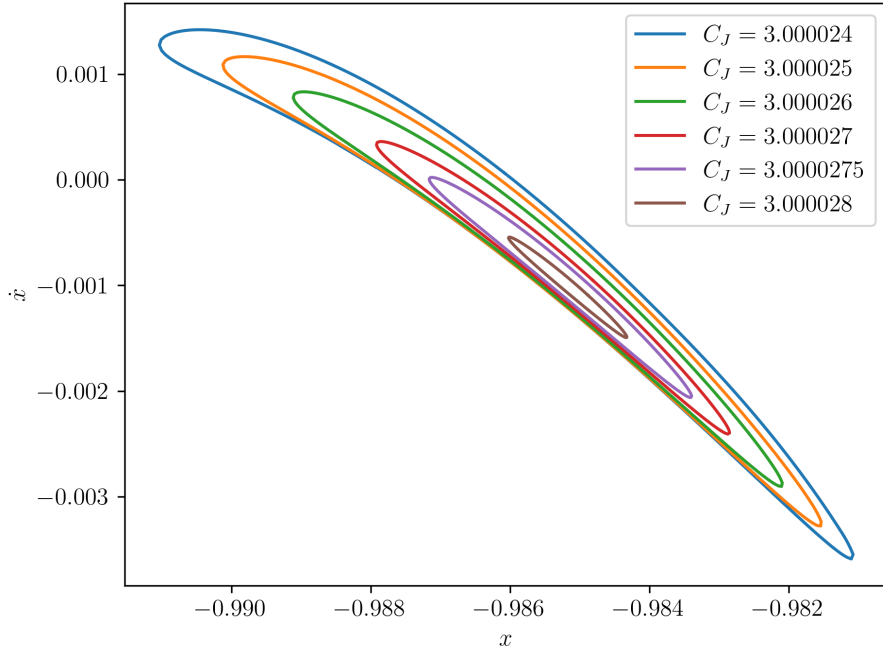


Figure 10: Projection (x, \dot{x}) of $\partial\mathcal{T}(c_J)|_\Sigma$ at section Σ for all $c_J \in \mathcal{C}$.

7.2 Impact simulations of planar transit orbits

7.2.1 Impact simulations at a fixed energy

This subsection numerically shows that for energy $c_J = 3.000027$, all initial conditions $(x, y, \dot{x}, \dot{y}) \in \mathcal{T}(3.000027)|_\Sigma$ generate transit orbits that eventually impact Phobos. In Figure 11, the projection of $\partial\mathcal{T}(c_J)|_\Sigma$ onto the (x, \dot{x}) -space (blue curve) encompasses the projection of $\mathcal{T}(3.000027)|_\Sigma$ onto the (x, \dot{x}) -space (orange points). Figure 12 then shows how all of these initial conditions give rise to transit orbits that impact Phobos.

This numerical example supports the claim that all orbits contained inside $\mathcal{W}^s(M|\mathcal{L}_H(c_J))$ are transit orbits that ultimately impact Phobos. This procedure has been repeated for all six energies in \mathcal{C} , and in each case, the initial conditions in $\mathcal{T}(c_J)|_\Sigma$ resulted in impacts on Phobos after numerical integration. The results for all six different energies c_J is presented in the next subsection.

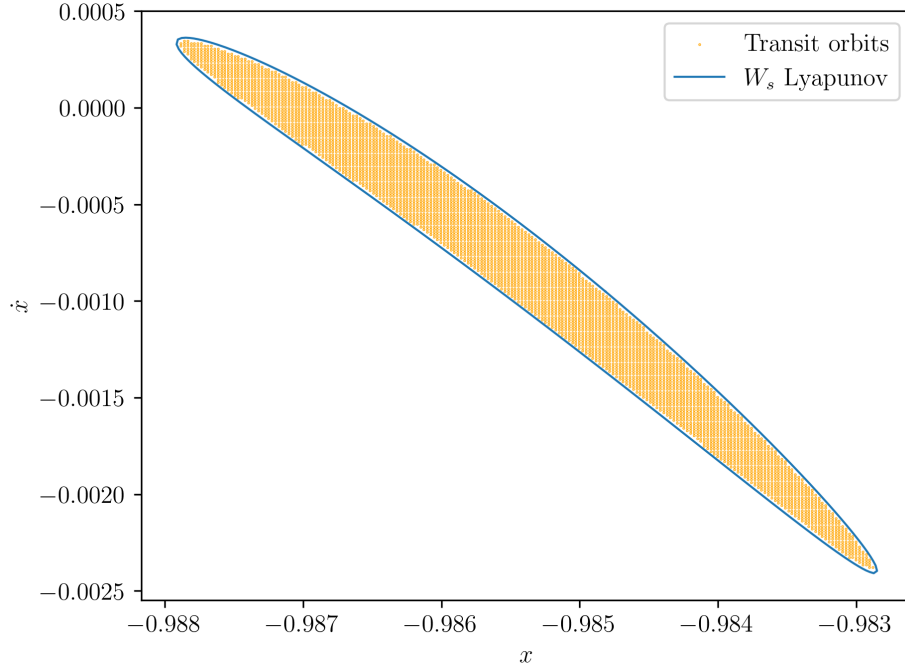


Figure 11: The blue curve is the projection onto the (x, \dot{x}) -space of $\partial\mathcal{T}(3.000027)|_{\Sigma}$. The 5000 (x, \dot{x}) coordinates of the initial conditions of planar transit orbits at $y = 0.04$, denoted by $\mathcal{T}(3.000027)|_{\Sigma}$ are represented by orange points.

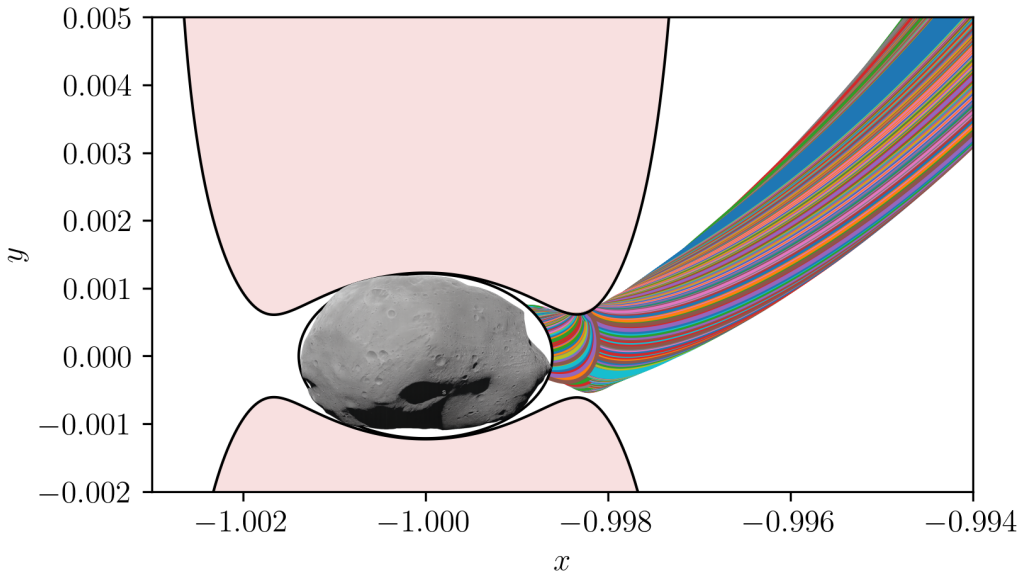


Figure 12: Planar transit orbits $\mathcal{T}(3.000027)$ impacting Phobos. Red-filled contours are forbidden regions for particles delimited by ZVCs.

7.2.2 Impact simulation at different energies

Figure 13 displays the impact coordinates (x, y) such that $(x, y, \dot{x}, \dot{y}) \in \mathcal{I}(c_J)$ for all $c_J \in \mathcal{C}$, where \dot{x} and \dot{y} are the associated impact velocities of (x, y) . The majority of impacts lie close to Stickney crater, which suggests a possible connection between the impacts of transit orbits $\mathcal{I}(c_J)$ and the crater's location. While coordinates $(x, y) \in \mathcal{I}(c_J)$ are more localized for higher values of c_J , the impact region extends when c_J decreases. This is consistent with

the fact that higher c_J correspond to smaller horizontal Lyapunov orbits $\mathcal{L}_H(c_J)$, resulting in narrower invariant stable and unstable manifolds, and a tighter bottleneck formed between Mars' region and Phobos' region by the ZVC.

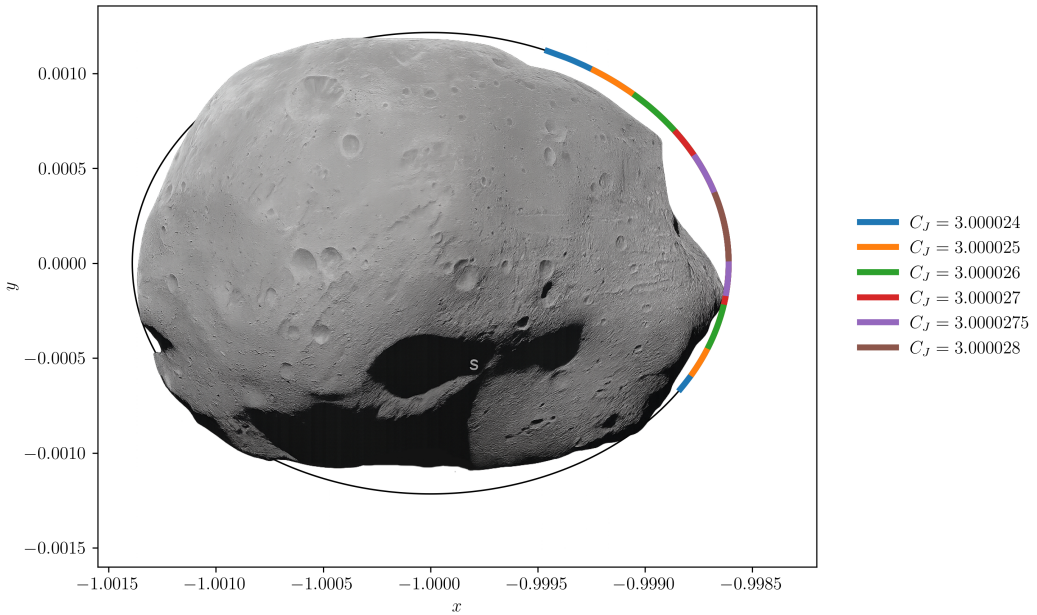


Figure 13: (x, y) -projection of $\mathcal{I}(c_J)$ for $c_J \in \mathcal{C}$.

In addition, Figure 14 depicts a histogram displaying the y coordinates of impact points $\mathcal{I}(c_J)$. The distribution is clearly non-uniform and asymmetrical, with a notable peak at $y \approx 0.0002$. Therefore, the distribution of impacts of transit orbits on Phobos' surface provides numerical evidence that supports the claim that Martian ejecta could have contributed to the current morphology of the Stickney crater on Phobos by traveling through invariant manifolds.

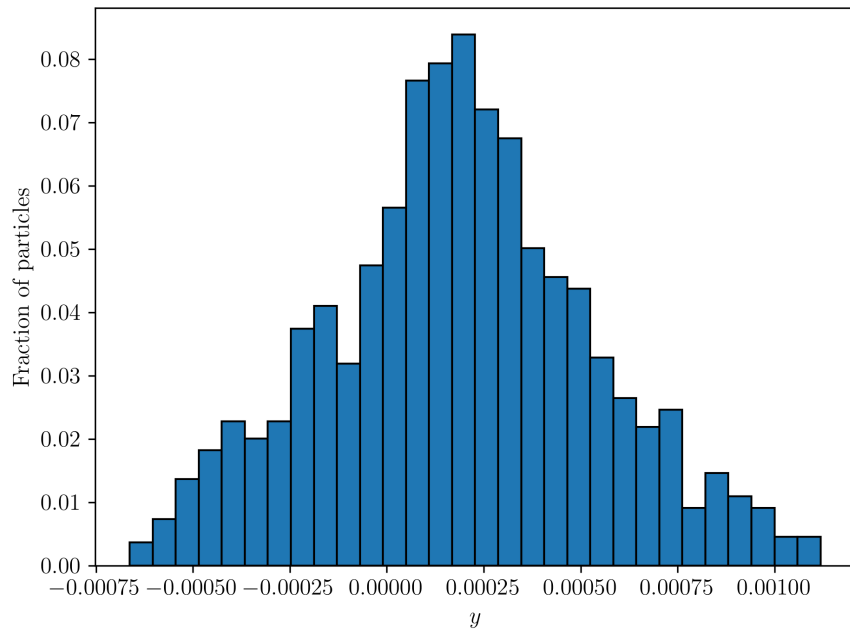


Figure 14: Histogram of y -coordinates of impacts on Phobos. It takes into account all $\mathcal{I}(c_J)$ for $c_J \in \mathcal{C}$ together. It has a total of 30000 impact points.

8 Conclusions

Based on the numerical simulations of low-energy planar transit orbits and the analysis of their impact conditions on Phobos, the results obtained within the theoretical framework of this thesis support the plausibility of a natural transport mechanism influencing the observed crater location. Therefore, sustained bombardment of dust particles on Phobos, originated by Martian ejecta and occurring over an extended period of time, could have contributed to the current morphology of the Stickney crater.

All the objectives of this thesis have been achieved. I have gained a solid understanding of the topology of the invariant manifolds that act as natural transfer pathways between Mars' region and Phobos' region, as well as the different types of motion that arise near the L_1 equilibrium point of the Mars-Phobos system. In this particular case, numerical simulations have shown that the invariant manifolds near L_1 form 2-dimensional tubes that contain transit orbits, all of which ultimately impact Phobos. I have also learned to apply the parameterization method to compute higher-order approximations of invariant manifolds near L_1 , and I have developed proficiency in the numerical integration of differential equations using Python.

For future work, the density of dust particles for different energy levels should be quantified, as this would make the estimation of the actual number of dust particles impacting Phobos possible. Once these calculations are available, crater physics should be pursued to further understand the physical consequences of such impacts. In addition, non-planar transit orbits and an accurate 3D model of Phobos should be considered.

9 Appendices

9.1 Linearization of F and diagonalization of $DF(0)$

The nonlinear terms of Eq (5) are expanded to a power series using the expressions provided in (Jorba et al. 1999), leading to the following reformulation of the equations of motion:

$$\begin{aligned}\ddot{x} - 2\dot{y} - (1 + 2c_2)x &= \frac{\partial}{\partial x} \sum_{n \geq 3} c_n(\mu) R^n P_n \left(\frac{x}{R} \right), \\ \ddot{y} + 2\dot{x} + (c_2 - 1)y &= \frac{\partial}{\partial y} \sum_{n \geq 3} c_n(\mu) R^n P_n \left(\frac{x}{R} \right), \\ \ddot{z} + c_2 z &= \frac{\partial}{\partial z} \sum_{n \geq 3} c_n(\mu) R^n P_n \left(\frac{x}{R} \right),\end{aligned}\quad (32)$$

where $R^2 = x^2 + y^2 + z^2$, P_n is the Legendre polynomial of degree n and the coefficients $c_n(\mu)$ for equilibrium point L_1 are also defined in (Jorba et al. 1999). The system of equations in Eq (32) can then be rewritten as an autonomous nonlinear system of differential equations such as $\dot{X} = F(X)$, where $X = (x, p_x, y, p_y, z, p_z)$, and F is the vector field of the equations of motion of the CR3BP expanded around L_1 . After some algebraic manipulations, the Jacobian matrix of F calculated at the origin is:

$$A = DF(0) = \begin{pmatrix} 0 & 1 & 1 & 0 & 0 & 0 \\ 2c_2 & 0 & 0 & 1 & 0 & 0 \\ -1 & 0 & 0 & 1 & 0 & 0 \\ 0 & -1 & -c_2 & 0 & 0 & 0 \\ 0 & 0 & 0 & 0 & 0 & 1 \\ 0 & 0 & 0 & 0 & -c_2 & 0 \end{pmatrix} \quad (33)$$

To analyze the linearized dynamics of F around L_1 , the eigenvalues and eigenvectors of A must be calculated. Note that A is a block-diagonal matrix that separates the planar motion (x, p_x, y, p_y) and the vertical motion (z, p_z) , as there is a top left 4×4 submatrix and a 2×2 bottom right submatrix. As a result, the eigenvalues and eigenvectors of each submatrix can be calculated independently, and then the 6-dimensional eigenvectors can be constructed by combining the corresponding planar and vertical components.

Planar motion

This subsection employs a method inspired by the approach presented in Section 2.1 of (Jorba et al. 1999). Let A^P be the top left 4×4 submatrix of A . Subtracting λ from its diagonal entries the following matrix is obtained:

$$A_\lambda^P = \begin{pmatrix} -\lambda & 1 & 1 & 0 \\ 2c_2 & -\lambda & 0 & 1 \\ -1 & 0 & -\lambda & 1 \\ 0 & -1 & -c_2 & -\lambda \end{pmatrix}.$$

The characteristic polynomial of A_λ^P is $p_P(\lambda) = \lambda^4 + (2 - c_2)\lambda^2 + 1 + c_2 - 2c_2^2$. Let $\eta = \lambda^2$. Then the solutions to the quadratic equation $p_P(\eta)$ are:

$$\eta_{2,1} = \frac{c_2 - 2 \pm \sqrt{9c_2^2 - 8c_2}}{2}, \quad (34)$$

where $\eta_2 > 0$ corresponds to the positive sign and $\eta_1 < 0$ corresponds to the negative sign in the previous equation. Therefore, we can define $w_h = \sqrt{|\eta_1|}$ and $\lambda_0 = \sqrt{\eta_2}$ so that $w_hi, -w_hi, \lambda_0, -\lambda_0$ are eigenvalues of matrix $DF(0)$. To find their corresponding eigenvectors, it is important to highlight that matrix A_λ^P can be written in the following way:

$$A_\lambda^P = \begin{pmatrix} B_\lambda^P & I_2 \\ -I_2 & C_\lambda^P \end{pmatrix}, \quad B_\lambda^P = \begin{pmatrix} -\lambda & 1 \\ 2c_2 & -\lambda \end{pmatrix}, \quad C_\lambda^P = \begin{pmatrix} -\lambda & 1 \\ -c_2 & -\lambda \end{pmatrix}. \quad (35)$$

To find the kernel of matrix A_λ^P , vector $v_\lambda = (v_1, v_2)$ is used, with $v_1 = (v_{11}, v_{12})$ and $v_2 = (v_{21}, v_{22})$. As a result, we have that $(C_\lambda^P B_\lambda^P + I_2)v_1 = 0$. From this equation, the following relationship between components v_{11} and v_{12} is obtained:

$$v_{12} = \frac{\lambda^2 + 2c_2 + 1}{2\lambda} v_{11}. \quad (36)$$

Additionally, $v_2 = -B_\lambda^P v_1$. Consequently, the eigenvector corresponding to eigenvalue λ has the following structure:

$$v_\lambda = (2\lambda, \lambda^2 + 2c_2 + 1, \lambda^2 - 2c_2 - 1, \lambda^3 + (1 - 2c_2)\lambda). \quad (37)$$

Vertical motion

Let A^V be the bottom right 2×2 submatrix of A . Its characteristic polynomial is $p_V(\lambda) = \lambda^2 + c_2$. Therefore, the eigenvalues are $w_v i, -w_v i$ with $w_v = \sqrt{c_2}$. Their corresponding eigenvectors are $(1, 0), (0, 1)$.

Eigenvalues and eigenvectors of A

The eigenvalues of A are $\lambda_0, -\lambda_0, w_hi, -w_hi, w_v i, -w_v i$, and their respective eigenvectors are:

$$E_A = \{(v_{\lambda_0}, 0, 0), (v_{-\lambda_0}, 0, 0), (v_{w_hi}, 0, 0), (v_{-w_hi}, 0, 0), (0, 0, 0, 0, 1, 0), (0, 0, 0, 0, 0, 1)\}$$

From this point forward, the eigenvector of A associated with eigenvalue λ uses is denoted by u_λ .

9.2 Second order approximation of F

The truncated expressions of Eq (32) at $n = 3$ are:

$$\begin{aligned}\ddot{x} - 2\dot{y} - (1 + 2c_2)x &= 3c_3(2x^2 - y^2 - z^2)/2, \\ \ddot{y} + 2\dot{x} + (c_2 - 1)y &= -c_3xy, \\ \ddot{z} + c_2z &= -c_3xz.\end{aligned}$$

For the derivatives of x, y and z , we can just rearrange the definitions for momenta:

$$\dot{x} = p_x + y, \quad \dot{y} = -x + p_y, \quad \dot{z} = p_z.$$

Deriving the three different momenta we get:

$$\begin{aligned}\dot{p}_x &= \ddot{x} - \dot{y} = \ddot{x} - p_y + x = 2c_2x + p_y + \frac{3}{2}c_3(2x^2 - y^2 - z^2), \\ \dot{p}_y &= \ddot{y} + \dot{x} = -p_x - c_2y - 3c_3xy, \\ \dot{p}_z &= \ddot{z} = -c_2z - 3c_3xz.\end{aligned}$$

Finally, the second order approximation of vector field $F_{\leq 2}$ can be written as:

$$\begin{aligned}F_1(X) &= F_1(x, p_x, y, p_y, z, p_z) = (p_x + y, 2c_2x + p_y, -x + p_y, -p_x - c_2y, p_z, -c_2z)^t, \\ F_2(X) &= F_2(x, p_x, y, p_y, z, p_z) = (0, \frac{3}{2}c_3(2x^2 - y^2 - z^2), 0, -3c_3xy, 0, -3c_3xz)^t, \\ F_{\leq 2}(X) &= F_1(X) + F_2(X),\end{aligned}$$

where F_1 only has the linear terms and F_2 only has the second-order terms. Note that F_2 is nonzero only for the \dot{p}_x , \dot{p}_y and the \dot{p}_z entries.

9.3 Impact velocities

The total impact velocities are calculated with the following formula:

$$v_{\text{impact}}(\dot{x}, \dot{y}) = \sqrt{\dot{x}^2 + \dot{y}^2},$$

where \dot{x}, \dot{y} are impact velocities on Phobos. The nondimensional units of velocity are converted back to km/h so that the reader can better understand how fast these dust particles travel. Note that these velocities are given in the reference frame \mathfrak{R}_n .

Figure 15 shows the different impact velocity profiles $v(\dot{x}, \dot{y})$ for all $c_J \in \mathcal{C}$, considering trajectories whose impact conditions satisfy $(x, y, \dot{x}, \dot{y}) \in \mathcal{I}(c_J)$. Lower values of c_J result in higher impact velocities. Note that there is a significant difference between $c_J = 3.000028$ and $c_J = 3.000024$, from maximum impact velocities of 10 km/h to 18 km/h.

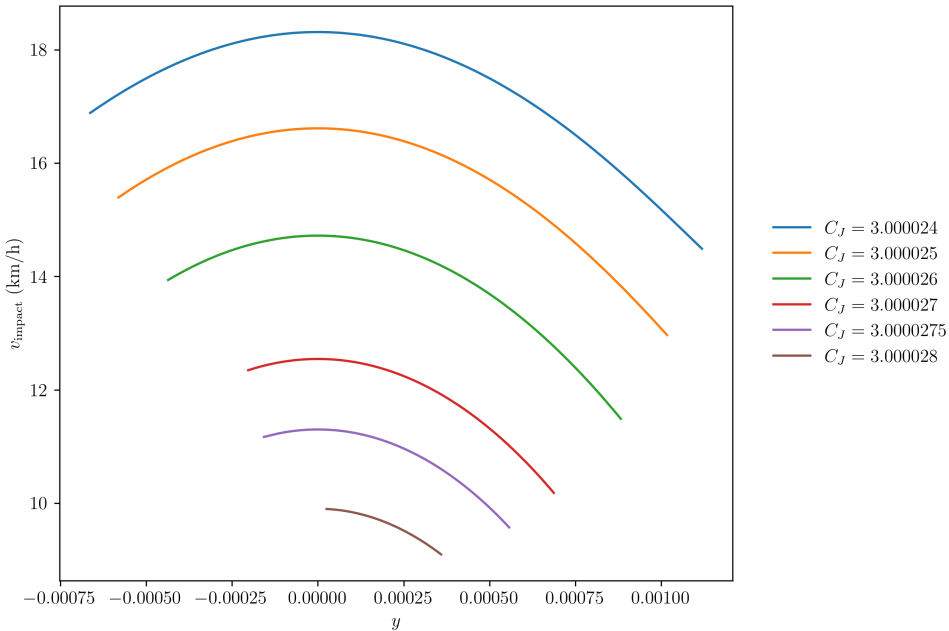


Figure 15: Impact velocities $v_{\text{impact}}(\dot{x}, \dot{y})$ in km/h for different values of y , where y, \dot{x} and \dot{y} are coordinates in $\mathcal{I}(c_J)$ for $c_J \in \mathcal{C}$.

References

- Abraham, R. and J. E. Marsden (1985). *Foundations of Mechanics*. 2nd. Addison-Wesley Advanced Book Program. Benjamin/Cummings.
- Chicone, C. (2006). *Ordinary Differential Equations with Applications*. 2nd. Vol. 34. Texts in Applied Mathematics. Springer.
- Gómez, G., À. Jorba, J. Masdemont, and C. Simó (1998). “Quasihalo Orbits Associated with Libration Points”. In: *Journal of Astronautical Sciences* 46.4, pp. 135–162.
- (2001). *Dynamics and Mission Design Near Libration Points. Volume III: Advanced Methods for Collinear Points*. Vol. 4. World Scientific Monograph Series in Mathematics. World Scientific.
- Gómez, G., W. S. Koon, M. W. Lo, J. E. Marsden, J. Masdemont, and S. D. Ross (2004). “Connecting orbits and invariant manifolds in the spatial three-body problem”. In: *Nonlinearity* 17.5, pp. 1571–1606.
- Gómez, G. and J. Mondelo (2001). “The dynamics around the collinear equilibrium points of the RTBP”. In: *Physica D: Nonlinear Phenomena* 157.4, pp. 283–321.
- Guckenheimer, J. and P. Holmes (1983). *Nonlinear Oscillations, Dynamical Systems, and Bifurcations of Vector Fields*. Vol. 42. Applied Mathematical Sciences. Springer-Verlag.
- Haro, À., M. Canadell, J.-L. Figueras, A. Luque, and J. Mondelo (2016). *The Parameterization Method for Invariant Manifolds: From Rigorous Results to Effective Computations*. Vol. 195. Applied Mathematical Sciences. Springer.
- Jorba, À. and J. Masdemont (1999). “Dynamics in the center manifold of the collinear points of the restricted three body problem”. In: *Physica D: Nonlinear Phenomena* 132.1, pp. 189–213.
- Koon, W. S., M. W. Lo, J. E. Marsden, and S. D. Ross (2022). *Dynamical Systems, the Three-Body Problem and Space Mission Design*. Marsden Books.
- Morbidelli, F. (2023). “Origin of Phobos grooves by Martian ejecta flying on low-energy trajectories”. Master’s Thesis. Politecnico di Milano.
- NASA (2013). *Phobos: Overview*. https://web.archive.org/web/20131019162634/http://solarsystem.nasa.gov/planets/profile.cfm?Object=Mar_Phobos&Display=Facts. Accessed via the Internet Archive on June 7, 2025. URL: https://web.archive.org/web/20131019162634/http://solarsystem.nasa.gov/planets/profile.cfm?Object=Mar_Phobos&Display=Facts.
- NASA/JPL/University of Arizona (2008). *Phobos Full-disk Image*. <https://photojournal.jpl.nasa.gov/catalog/PIA10368>. NASA Planetary Photojournal. URL: <https://photojournal.jpl.nasa.gov/catalog/PIA10368>.
- Poincaré, H. (1887). *Sur le Problème des Trois Corps et les Équations de la Dynamique*. Acta Mathematica.
- Ramsley, K. R. and J. W. Head (2021). “The Origins and Geological Histories of Deimos and Phobos: Hypotheses and Open Questions”. In: *Space Science Reviews* 217.8.
- Szebehely, V. (1967). *Theory of Orbits: The Restricted Problem of Three Bodies*. Academic Press.